

**High-resolution cryoEM structure determination of soluble proteins after soft-landing electrospray ion beam deposition.**

Lukas Eriksson,<sup>1,2</sup> Tim K. Esser,<sup>1, a)</sup> Marko Grabarics,<sup>1,2</sup> Laurence T. Seeley,<sup>1,2,3</sup> Simon B. Knoblauch,<sup>1,2</sup> Jingjin Fan,<sup>1,2</sup> Joseph Gault,<sup>2, b)</sup> Paul Fremdling,<sup>2, c)</sup> Thomas Reynolds,<sup>4</sup> Justin L.P. Benesch,<sup>1,2</sup> Carol V. Robinson,<sup>1,2</sup> Jani R. Bolla,<sup>4</sup> Lindsay Baker,<sup>1,3</sup> and Stephan Rauschenbach<sup>1,2</sup>

<sup>1)</sup>*Kavli Institute for Nanoscience Discovery, Dorothy Crowfoot Hodgkin Building, University of Oxford, South Parks Road, Oxford OX1 3QU,*

*UK*

<sup>2)</sup>*Department of Chemistry, University of Oxford, Mansfield Road, Oxford OX1 3TA,*

*UK*

<sup>3)</sup>*Department of Biochemistry, University of Oxford, South Parks Road, Oxford OX1 3QU,*

*UK*

<sup>4)</sup>*Department of Biology, University of Oxford, South Parks Road, Oxford OX1 3RB,*

*UK*

(\*Electronic mail: [stephan.rauschenbach@chem.ox.ac.uk](mailto:stephan.rauschenbach@chem.ox.ac.uk))

(Dated: 23 March 2026)

Electrospray ion beam deposition (ESIBD) is the intact, chemically selective deposition of molecular ions on surfaces in vacuum. Here, we present a general method and dedicated instrumentation for ESIBD-based cryoEM sample preparation of soluble proteins. Precise control over deposition energy, sample environment, and reproducible growth of thin, homogeneous, vitreous ice films embedding the deposited proteins results in samples suitable for high-resolution cryoEM structure determination. Applied to several protein complexes,  $\beta$ -Galactosidase, GDH, RuBisCo, GroEL, the workflow yields near-atomic resolution cryoEM maps (2.5–4.8 Å) from which atomic models are derived. Dehydration-induced structural changes correlate with the magnitude of solvent exposure in the native structure: interior residues present high-resolution density while surface-exposed regions rearrange. Coherent rearrangements retain secondary and tertiary structure, incoherent changes degrade resolution. These results establish ESIBD+cryoEM as viable method for structure determination of chemically selected protein samples, directly linking native MS chemical information with near-atomic structural resolution.

---

<sup>a)</sup>Currently at Thermo Fisher Scientific, De Schakel 2, 5651GH Eindhoven, Netherlands

<sup>b)</sup>Currently at AstraZenica, Discovery Sciences, Biopharma R&D, Cambridge CB2 0AA, UK

<sup>c)</sup>Currently at REELEMENTS GmbH, Wilhelm-Eichler-Straße 34, 01445 Radebeul, Germany

## INTRODUCTION

Establishing the relationship between a protein's precise chemical identity, its structure (at high resolution), and its interactions is considered central to many questions in molecular biology, (patho)physiology, and drug discovery.<sup>1,2</sup> To this end, high performance analytical methods are widely employed. Most prominent among them are (native) mass spectrometry (MS)<sup>1,3,4</sup> for obtaining chemical information and electron cryo-microscopy (cryoEM),<sup>5,6</sup> which recently became a primary tool for structure determination. Native MS, based on the intact ionisation of entire protein complexes with ligands by native electrospray ionisation (native ESI), excels at determining stoichiometry and interactions. CryoEM, on the other hand, extracts near-atomically resolved structures of proteins by averaging over many particles picked from micrographs of a sufficiently purified, i.e., homogeneous protein sample.

While high-resolution MS can discern protein sequence, binding, stoichiometry, interaction strength, or heterogeneity of a protein sample,<sup>7</sup> information about their three-dimensional structure can only be extracted at low spatial resolution when native MS is combined with methods such as ion mobility spectrometry or hydrogen-deuterium exchange.<sup>8,9</sup> On the other hand, cryoEM, which often requires extensive purification to obtain samples of homogeneity sufficient for high spatial resolution reconstructions, cannot always replicate the chemical versatility that can be mapped by MS.

Soft-landing electrospray ion beam deposition (ESIBD), i.e., the gentle deposition of intact molecular ions onto surfaces in vacuum, has attracted attention because of its potential to provide a direct link between the chemical information from MS and high-resolution spatial information from high-resolution microscopy.<sup>10</sup> In ESIBD, MS is used for sample preparation: Intact molecular, gas-phase ions generated by native ESI are transferred into vacuum, purified chemically by mass-filtering, and gently deposited onto surfaces in vacuum—a precisely controlled process which ensures chemical purity and homogeneity of the prepared samples, as demonstrated extensively in sample fabrication for scanning probe microscopy.<sup>10–12</sup>

Recently, we implemented ESIBD for electron microscopy<sup>13</sup> demonstrating the principal feasibility of combining ESIBD and cryoEM for high-resolution cryoEM imaging of the protein  $\beta$ -Galactosidase. When prepared using native ESI, the secondary structure and overall shape and fold were retained when ensuring gentle deposition<sup>14,15</sup> and embedding the protein in a thin ice film.<sup>16</sup> However, small rearrangement of domains and a loss of resolution at the protein surface

due to the dehydration in the ESI process was observed. From these experiments alone, it was unclear whether this approach could be generalised as a viable method for high-resolution protein structure determination. These initial experiments also revealed several shortcomings of the prototype instrumentation and workflow: Due to a lack of precise control, the embedding of the proteins via ice growth in vacuum was inconsistent. The proteins were embedded within polycrystalline ice that varied extensively in thickness and morphology, which affected cryoEM data collection efficiency. Further, the pivotal vacuum-liquid nitrogen transfer from ESIBD to cryoEM was inconsistent and prone to contamination.

Here, we present novel instrumentation for ESIBD sample preparation and a general method for its application, optimised towards high-resolution cryoEM imaging of soluble proteins. We developed deposition and sample handling instrumentation that ensures the fully controlled, gentle, and contamination-free deposition of proteins onto cryoEM grids in vacuum. Essential to this experiment was ensuring the embedding of proteins into an ultrathin, amorphous, homogeneous ice film, for which we establish a robust and reproducible method. Based on this method, we show high resolution imaging for several proteins— $\beta$ -Galactosidase, GDH, RuBisCo, and GroEL—and for each derive atomic models. Obtaining high-resolution structures enabled us to understand the mechanisms that govern the retention and/or changes in protein structure from dehydration in the ESI process and determine the properties of the protein that govern it, offering potential routes to control or reverse these structural changes.<sup>17</sup>

## RESULTS

### Instrumentation and Workflow

For ESIBD experiments, we use a modified Thermo Scientific Q Exactive UHMR instrument,<sup>15</sup> extended by two differential pumping stages containing electrostatic lenses and deposition instrumentation at a pressure reaching ultrahigh vacuum (UHV,  $p < 10^{-9}$  mbar, see Fig. 1a). A deposition extension like this can be fitted, in principle, to any typical native ESI-MS instrumentation such that the workflow presented in the following can be applied for high-resolution microscopy, e.g., scanning probe microscopy (SPM)<sup>10,18,19</sup> or electron cryo-microscopy (cryoEM),<sup>20</sup> sample fabrication for other methods, or for material fabrication.<sup>21-23</sup>

In our ESIBD setup, a beam of molecular ions generated by native ESI is mass-to-charge-ratio

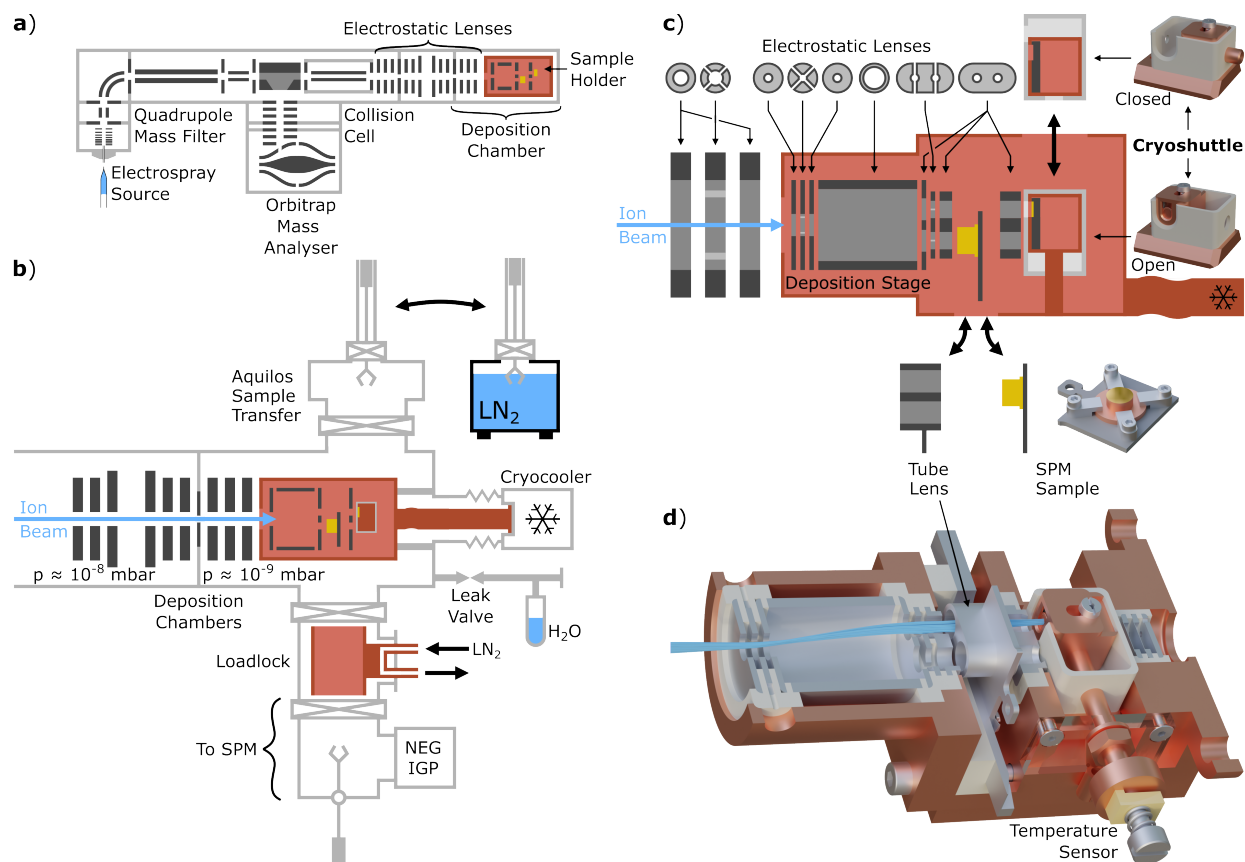


**FIG. 1. Instrumentation Overview.** **a)** Schematic of the deposition instrument based on a modified Orbitrap UHMR. **b)** Schematic of the deposition chamber containing the cryogenic sample stage and sample transfer systems for cryoEM and SPM samples. **c)** Cross section schematic of the cryogenic deposition stage. Cryoshuttle shown in both states: deposition (open) and transfer (closed). **d)** Section-view rendering of the deposition stage with simulated ion trajectories (blue) for deposition onto a cryoEM grid. Tube lens inserted into SPM sample holder position.

( $m/z$ )-filtered, characterised by MS, and then passed through an aperture at the exit of the collision cell. From this point onwards, the ion beam has a well-defined chemical composition as well as spatial and energy distribution. The beam is controlled using electrostatic (DC) ion optics (Fig. 1) which steer and focus the beam.

Within the deposition stage, lenses steer the ion beam onto cryoEM grids held within a cryoshuttle (Fig. 1c) or onto single crystal surfaces for SPM imaging (see SI for details on SPM capabilities) where the landing energy is defined in a range from 1 eV to above 100 eV by biasing the sample.<sup>15</sup> When depositing proteins onto cryoEM grids, the SPM sample is replaced by a tube lens mounted on an SPM sample plate (Fig. 1c,d) to maintain a well-defined potential for beam

transmission over the void space (Fig. 1d). The intensities of the ion beam impinging on apertures and at the sample are measured as currents by picoammeters, which aid alignment and focusing of the ion beam and allow for a precise quantification of the amount of deposited proteins.

For structure determination by cryoEM, it is crucial that the sample is kept at a consistent, cryogenic temperature to avoid thermal activation, because it can cause structural heterogeneity and hence loss of resolution.<sup>16,24</sup> A cryo-vacuum environment further maintains sample cleanliness,<sup>25</sup> enables control over ice growth,<sup>26</sup> and limits mobility of molecules on surfaces.<sup>27</sup> At the deposition stage, a reverse Stirling cryocooler (Sunpower Cryotel GTLT, Fig. 1b) provides cooling; temperature sensors, a resistive heating element, and a temperature controller (Lake Shore Model 335) allow for precise temperature regulation, keeping the cryoshuttle within 10 mK of a user-defined setpoint between 60 K and 350 K.

To minimise sample contamination by adsorption of residual gases during the deposition process, especially of a cold sample, the deposition stage is designed such that sample surfaces do not have direct line of sight to any room temperature surfaces. In the deposition section, UHV ( $p = 10^{-9}$  mbar) is achieved in the second differentially pumped chamber downstream of the mass spectrometer (Fig. 1b). In addition, when the cryo-stage is running, it functions as a cryopump, further decreasing the pressure in the chamber to  $5 \times 10^{-10}$  mbar and even lower at the sample position which is completely surrounded by cold surfaces.<sup>25</sup> After successful ion beam deposition, the landed protein molecules can be embedded in ice by growing a film from water vapour leaked into the deposition chamber at a defined partial pressure.

To protect cryoEM grids from contamination during transfer, a cryoshuttle, compatible with Thermo Scientific's Aquilos transfer hardware, is employed. After cryoEM sample preparation at 115 K, the shuttle is further cooled to 93 K to compensate for any warming that may occur during transfer. The transfer temperature is kept well below the devitrification temperature of ice,  $T > T_g \approx 136$  K,<sup>26,28</sup> which varies with film thickness<sup>29</sup> and pressure,<sup>30</sup> and is also likely influenced by the substrate, including the presence of contamination or protein adsorbates. During transfer, grids are protected by PEEK shutters which automatically close when the shuttle is removed from the deposition position (see Fig. 1c, suppl. movie S1). The shuttle is extracted from UHV into a small chamber, transferred under static vacuum, and vented through clean nitrogen gas into liquid nitrogen (Fig. 1b).<sup>16</sup> This process typically takes less than one minute, during which contamination from atmospheric ice is minimised and the grids maintain a temperature below  $T_g$  such that devitrification is avoided.

## Ice growth on TEM grids

Conventional cryoEM sample preparation by plunge freezing yields proteins embedded in a thin, vitreous layer of ice.<sup>31</sup> Critically, for particles to be distinguishable in the acquired micrographs, the ice must be sufficiently thin, in the range of 10 nm to 50 nm, and homogeneous in phase and morphology.<sup>32</sup>

Proteins prepared by ESIBD adsorb on the surface of the substrate, typically an ultrathin membrane of amorphous carbon,<sup>33</sup> in vacuum. Due to the absence of ice, these proteins show very high contrast in micrographs, as seen in Fig. 2a. The 2D classes and 3D reconstructions of ice-free, ESIBD-prepared proteins show the correct size and shape, but an unresolved shell at the surface of the protein makes the determination of structural features at high resolution impossible.<sup>33</sup> When an ice film is grown over the landed proteins, such a shell is not observed in 3D reconstructions and the resolution is improved overall, allowing the structure of the entire protein to be determined.<sup>16</sup>

The optimal ice layer is thin, flat, and homogeneous to maximise contrast and optimise consistency of particle picking and refinement. Crucially, the ice is vitreous, i.e., low density amorphous,<sup>31,34</sup> so that proteins are not obscured by contrast from features such as ice crystal grains.

In our instrument, we grow ice films on TEM grids by condensing water vapour onto the surface of a free-standing amorphous carbon film at a defined, low temperature while the sample is in the deposition stage and the shutter is open. After the landing of protein molecules onto a substrate at low temperatures, the deposition stage is held at a defined temperature for ice growth, typically 115 K, at a base pressure of  $10^{-9}$  mbar. A leak-valve to a reservoir containing liquid water and water vapour at equilibrium (at room temperature) is opened, raising the partial pressure of water in the chamber to a defined value, typically  $5 \times 10^{-5}$  mbar. By adjusting the pressure, we define the flux of water molecules towards the surface, i.e., the rate of ice film growth. As the low-temperature stage acts as a cryopump, the partial pressure of water at the sample position inside the stage is estimated to be about two to three orders of magnitude lower than measured in the chamber, based on ice growth rates.<sup>26</sup> After a defined time, the valve is shut, and excess water vapour is pumped, reducing the partial pressure of water to a negligible amount and stopping the growth. After ice growth, the stage is cooled to 93 K, and the shuttle is transferred into liquid nitrogen using the Aquilos system, as previously described.<sup>16</sup>

To explore and optimise the control of the ice growth,  $\beta$ -Galactosidase was deposited onto 2 nm

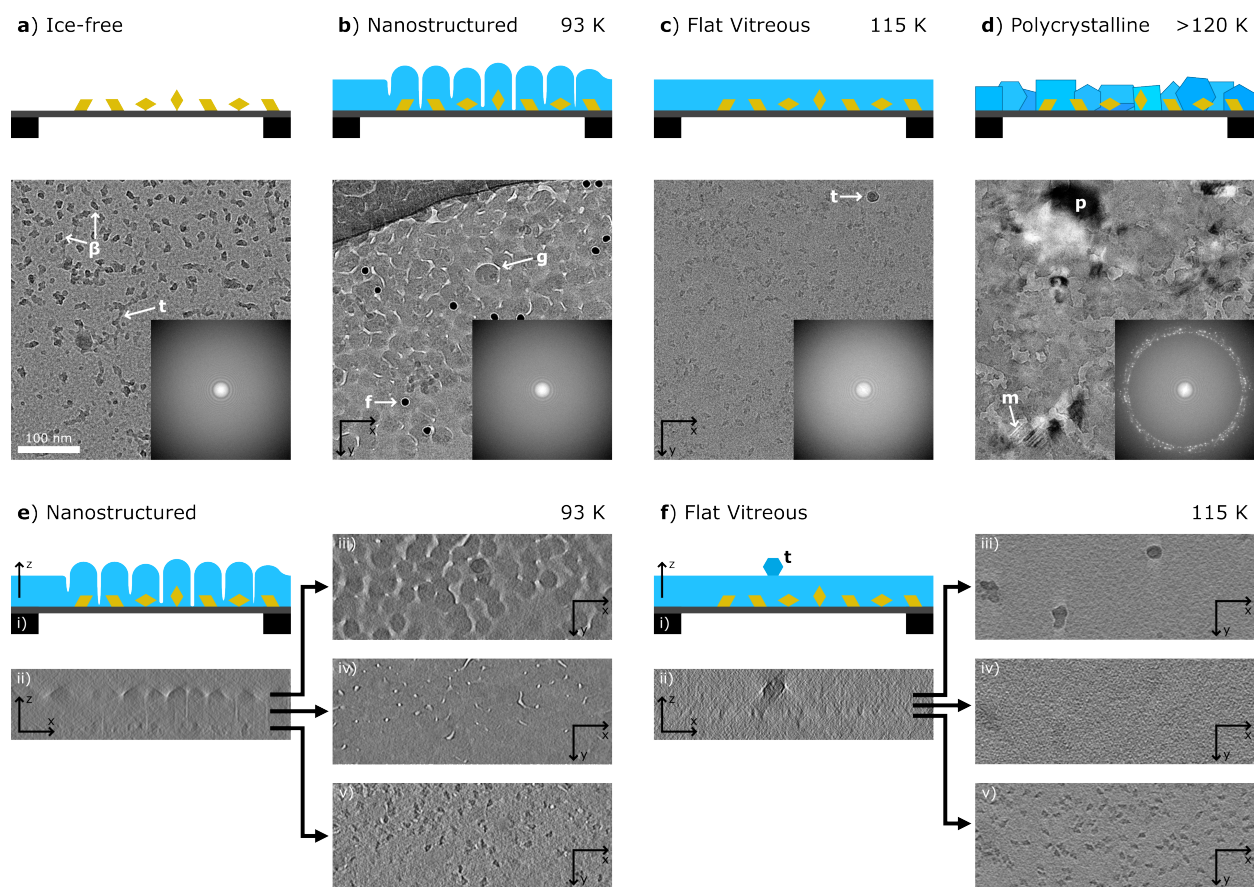


**FIG. 2. Control of ice phase and morphology.** **a-d)** Side view schematics, cryoEM micrographs, and inset power spectra of  $\beta$ -Galactosidase deposited on amorphous carbon films **a)** without ice deposition. **b)** Ice grown at 93 K. **c)** Ice grown at 115 K. **d)** Ice grown above 120 K. All ice was grown for 3 minutes at  $5 \times 10^{-5}$  mbar and all micrographs are at the same scale.  $\beta$ -galactosidase particles ( $\beta$ ), transfer ice contamination (t), gold fiducials (f), gaps (g), and features indicative of crystalline ice (p, m) are labelled. **e)** Schematic (i) and tomogram slices (ii-v) of nanostructured ice, grown at 93 K. Tomogram xz-slice shows columns of ice with rounded tops. Proteins can be seen towards the bottom as darker patches and in the xy-plane slice (v). The gaps between nanostructures appear as bright, vertical lines (in xz slice), and higher xy-slices show nanostructured ice and the rounded tops. **f)** Schematic (i) and tomographic slices (ii) xz, (iii-v) xz at various heights show evidence of a flat, vitreous ice film grown at 115 K embedding the proteins.

amorphous carbon film supported by TEM grids (Quantifoil). Ice was grown at various temperatures as described, and the samples were imaged by cryoEM, including tilt series for tomographic reconstruction. Figure 2a-d which shows a schematic cross section, representative micrograph, and inset power spectrum for each of the different conditions. Figure 2a shows a grid prepared

at cryogenic temperatures, but with no exposure to water vapour, i.e., without ice growth. High contrast between the characteristically-shaped  $\beta$ -Galactosidase particles ( $\beta$ ) and the background is observed. The background is indicative of the amorphous carbon layer. Small ice particles (t) are visible on the surface, arising from contamination during sample transfer and storage.

When ice is grown at a very low temperature, 93 K (Fig. 2b), the resulting micrographs show  $\beta$ -Galactosidase particles with much lower contrast compared to the ice-free sample (a). The very dark spots of contrast (f) are 10 nm gold fiducials, added to aid with tomogram reconstruction. All across the sample, we find rounded features of 30 nm diameter surrounded by bright, narrow edges of about 5 to 50 nm length (g), containing  $\beta$ -Galactosidase fully embedded in ice. The power spectrum without sharp diffraction features indicates that the ice is amorphous. Tomography (Fig. 2e) shows that the ice film grows atop the proteins as nanostructured columns with rounded tops, explaining the bright rims featured as thin, crevasse-like channels of vacuum between ice columns, likely a consequence of self-shadowed growth.<sup>35</sup>

After 115 K ice growth,  $\beta$ -Galactosidase particles are the main features visible in the micrographs (Fig. 2c). They are clearly visible yet at lower contrast than for the ice-free sample. The micrograph shown does not feature any bright or dark patches except one small ice crystal (t) due to contamination during sample transfer. The ice layer is vitreous as evidenced by the power spectrum, and it is  $\sim 20$  nm thick and homogeneous, as determined from cryoET (Fig. 2f).

Ice grown above 120 K (Fig. 2d) is polycrystalline, clearly identifiable by the bright and dark patches (p) and Moiré fringes (m), common features in cryoEM micrographs of polycrystalline ice.<sup>5,34,36,37</sup> Further, the power spectrum clearly shows many diffraction peaks, corresponding to the various, differently-oriented, and predominantly cubic crystalline domains in the micrograph. Protein particles are visible, but many are obscured by the features of the polycrystalline ice.

Clearly, for single particle analysis (SPA), the sample prepared at 115 K showing thin, flat, homogeneous vitreous ice is most suitable. The lack of other high-contrast features, coupled with good contrast between the particle and the background, makes particle picking and alignment easier. While particle contrast is not as high as in ice-free samples, resulting 3D reconstructions do not show a shell at the surface of the protein. The resolution of the cryoEM maps of ice-embedded proteins reached a level where models can be built at near-atomic resolution.<sup>16</sup> The additional features in the raw data from the polycrystalline and nanostructured amorphous ice mask the proteins in the micrograph to a point where particle picking for SPA is less efficient or impossible.

Overall, with precise control over the partial pressure of water vapour, stage temperature, and growth time, controlling the morphology and phase of the ice film is possible. With our optimised transfer into liquid nitrogen, samples can now be fabricated with consistent, optimal ice embedding.

### **ESIBD+cryoEM workflow for soluble proteins**

Using the procedure for deposition and consistent ice growth, we prepared samples of different soluble protein complexes to benchmark our approach:  $\beta$ -Galactosidase, a homotetrameric enzyme; Glutamate Dehydrogenase (GDH), a homohexameric enzyme; Ribulose-1,5-bisphosphate carboxylase/oxygenase (RuBisCo), a hetero-16-meric enzyme made up of 8 large subunits and 8 small subunits; and GroEL, a homo-14-meric chaperonin. Solutions of the proteins were prepared at 1 to 10  $\mu$ M concentration in 200 mM ammonium acetate (pH 6.9) then loaded into gold-coated nano-ESI emitters pulled from borosilicate glass capillaries, as standard for native MS.<sup>33</sup>

Conventionally, in analytical native MS, steps are often taken to narrow peak widths by desolvation and activation of the protein complex, removing adducts such as water molecules and buffer ions.<sup>3,7</sup> However, these conditions can thermally and collisionally excite the molecule.<sup>38,39</sup> Thus, for deposition, we tune the instrument for the most gentle spray and ion transport conditions. We set the capillary temperature to 50°C and apply no desolvation voltage, in-source trapping, or activation in the collision cell. This results in wide peaks (50-100 Th FWHM, Fig. 3) compared to many reported native mass spectra,<sup>26,40</sup> due to the variation in mass from residual water and other adducts, on the order of hundreds of molecules.

Once spray conditions are set, we first record the mass spectra of the proteins without any mass selection (Fig. 3). The desired species are then selected with the quadrupole mass filter (Fig. 1a), excluding impurities and undesired oligomers. For all proteins, the molecular peak of the intact complex of correct stoichiometry is the dominant peak, but contaminants are clearly present, making up approx. 50% of the integrated intensity. For  $\beta$ -Galactosidase and GDH, super-oligomers are the major impurities excluded, while for GroEL the most abundant impurity is the heptamer.

During deposition, the ions are guided through the collision cell by a gentle voltage gradient, where many low-energy ion-nitrogen collisions thermalise the ions, effectively narrowing the energy distribution of the ion beam to approximately 1 eV per charge FWHM,<sup>41</sup> which represents

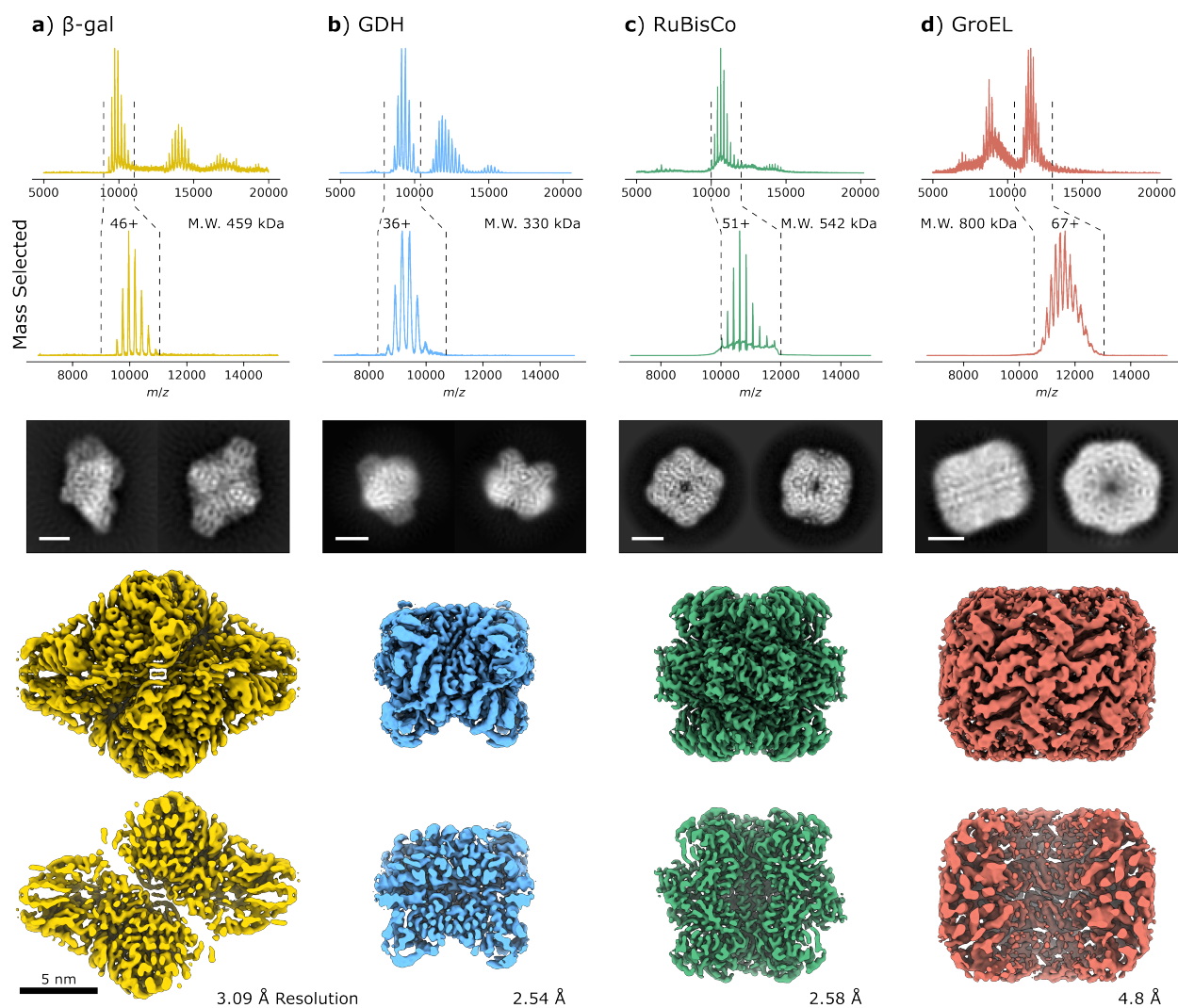


**FIG. 3. Mass spectra, 2D classes, and cryoEM maps of ESIBD-prepared soluble proteins.** Native MS shown before and after  $m/z$  selection (filter region indicated by dashed lines), representative 2D classes (scale bars 5 nm), and cryoEM density maps for  $\beta$ -Galactosidase (a), GDH (b), RuBisCo (c), and GroEL (d). Resolution values given at FSC 0.143 cutoff.

the lower limit achievable for the surface-molecule collision.<sup>15</sup> After thermalisation, the ion beam enters the high vacuum part of the ESIBD instrument (see Fig. 1), where no more collisions with gas molecules occur, which means that from this point on the beam energy is defined and will be conserved until deposition. Protein ion beams are typically centred in energy around -7 eV per charge, with values given with respect to ground (this means the beam column is biased more negatively to allow transmission). The ions are then directed to the grid for deposition which is held at a temperature of 115 K. For very gentle landing with collision energy of less than 2 eV

per charge, the voltage of the grid is typically set to -8.5 V. Typically, currents in the range of 20-50 pA at the sample are achieved after mass selection. The quantity deposited is monitored by integrating the deposition current over time; the deposited charge in the following is given in pAh (picoampere-hours).<sup>10</sup>

The tight energy distribution allows for effective focusing of the ion beam onto a small region of the surface, allowing for fast depositions resulting in reasonable particle density. We landed 11 pAh of  $\beta$ -Galactosidase, 15 pAh of GDH and GroEL, and 10 pAh of RuBisCo, or approximately 5 to 10 billion molecules in 15-45 minutes, resulting in roughly 4 mm<sup>2</sup> of the 7.8 mm<sup>2</sup> grid having optimal particle density for data collection (see suppl. eq. 1,2). An optimal density maximises the number of particles per micrograph without particles being so close together that they hamper alignment and particle picking. Ideally, particles will be spaced approximately one to two particle lengths away from all nearest neighbours, or 10 to 25% of monolayer coverage.

After protein deposition, ice was grown at 115 K and samples were transferred to storage in liquid nitrogen as described above. From here, the samples can be handled identically as samples prepared by plunge freezing: They are stored in liquid nitrogen until cryoEM imaging.

### **Structural analysis of ESIBD-prepared proteins**

We imaged the samples using typical microscope settings, and processed the resulting data with standard workflows (see methods/SI).<sup>42,43</sup> All proteins studied here, which vary in size, expression organism, and oligomeric stoichiometry, show 2D classes with characteristic features of  $\alpha$ -helices and  $\beta$ -sheets. The reconstructed consensus 3D maps (shown in Fig. 3), with symmetry (D2, D3, D4, and D7, respectively) imposed are high-resolution—all below 5 Å—suitable for building partial atomic models. Comparing the ESIBD-prepared 3D maps of all four proteins presented here to their plunge-frozen structures, we can make several key observations:

- i) The majority of secondary structure motifs as they are present in solution are reproduced in the structures obtained from ESIBD+cryoEM,
- ii) Local resolution is typically higher in the interior of the protein and lower at protein surfaces, but varies significantly across the protein surface,
- iii) Protein domains shift their location and orientation with respect to the solution structure, while internal structure is mostly unaltered.

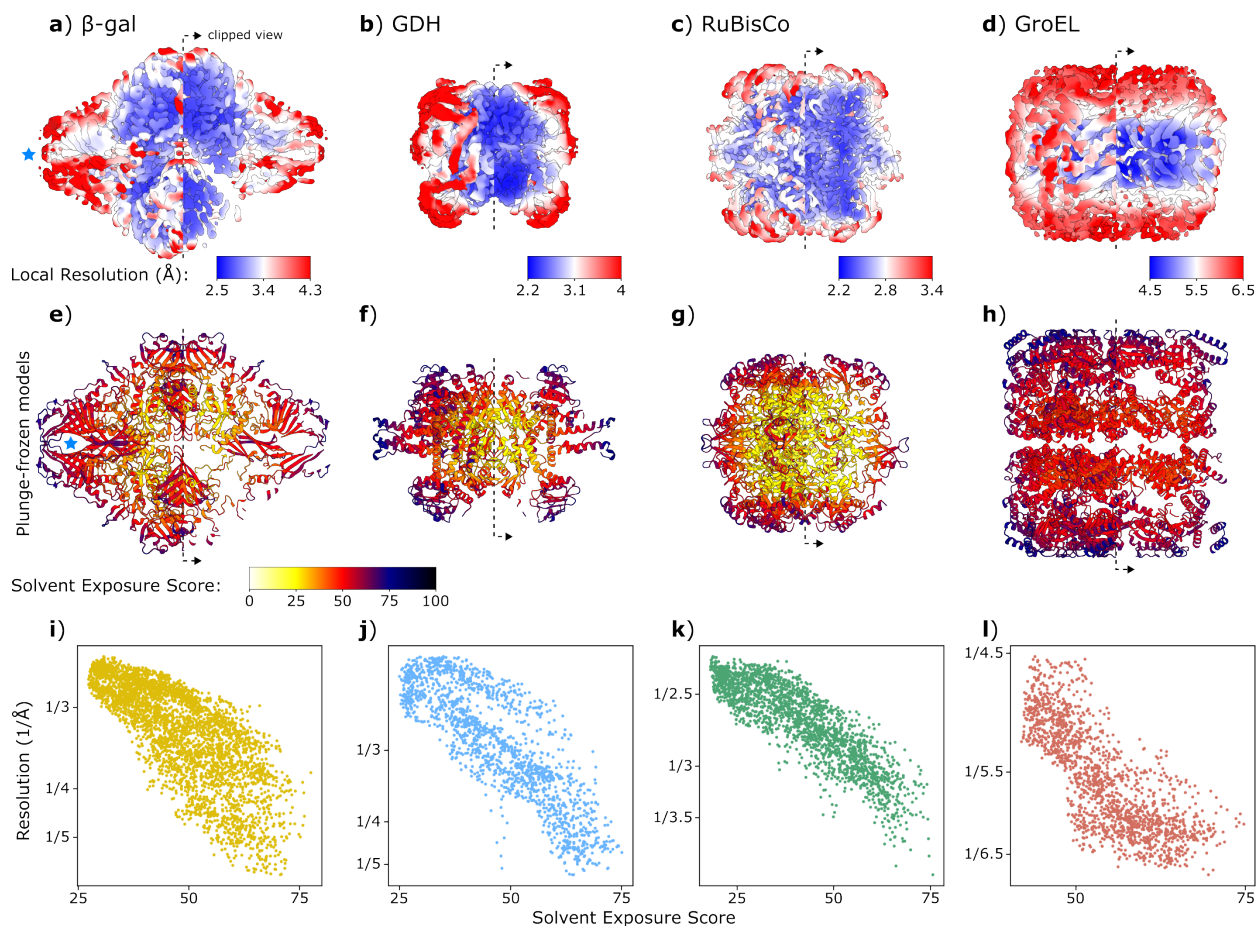


**FIG. 4. Local resolution trends in ESIBD-prepared proteins.** **a-d)** Consensus cryoEM maps of proteins prepared with ESIBD, coloured by local resolution (FSC cutoff 0.5). **e-h)** Solution phase models of proteins coloured by solvent exposure score. **i-l)** Plots of solvent exposure score (from solution phase model) versus local resolution for all backbone atoms modelled in ESIBD-prepared proteins. Individual maps, models, and plots for  $\beta$ -Galactosidase, GDH, RuBisCo, and GroEL. A blue star marks the location of a crevice which collapses in the gas phase.

In Fig. 4, we overlaid local resolution onto the density maps of ESIBD-prepared proteins. High resolution in the interior and a lower, but varying, local resolution across the surface of the protein has been observed in our proof-of-principle experiments on  $\beta$ -Galactosidase<sup>16</sup> and holds true for all maps generated for soluble proteins prepared by ESIBD. For  $\beta$ -Galactosidase, GDH, and RuBisCo, resolution of the core regions range from 2.2 to 3.5 Å, while GroEL is lower resolution, approximately 4.5 to 6.5 Å.

Generally, regions of the protein with greater exposure to solvent in their native state show lower local resolution in maps generated by ESIBD+cryoEM. These are regions of the protein

where a greater proportion of their local, non-covalent interactions are with solvent molecules—through hydrogen bonds, polar/ionic interactions, and van der Waals interactions. Upon ESI and subsequent dehydration, these interactions are removed. Additionally, the screening of electrostatic forces provided by water disappears, increasing the strength of Coulombic interactions such as hydrogen bonds, dipole-dipole, or ionic interactions.<sup>44</sup> As a consequence, the dehydrated protein in solution configuration is no longer at an energy minimum, most prominently at the previously solvent-exposed regions, and will therefore rearrange towards a new minimum energy configuration, for instance by forming new intra-molecular interactions where kinetically feasible.

To rationalise this observation, we introduce a solvent exposure score computed on plunge-frozen/crystal structures (see Methods for further details). For each residue/atom, this score estimates the share of non-covalent interactions with surrounding matter originating from solvent interactions, where a higher score indicates more interaction with the solvent. In Fig. 4e-h, we show plunge-frozen structures of  $\beta$ -Galactosidase, GDH, RuBisCo, and GroEL with residues colour-coded by the local solvent exposure score. We find that atoms/residues in the proteins' interiors yield a low score due to being surrounded mostly by other protein residues, whereas atoms at the protein surface have a high score, especially if located at an exposed, protruding site. For all examples shown, the protein exposure score aligns with the local resolution excellently, as underpinned in the correlation plots shown in Fig. 4i-l.

In particular, the solvent exposure score also mirrors the variation in local resolution across the surface of the proteins. For instance, the inside of the cavity of RuBisCo, which is reproduced at high resolution ( $<2.5$  Å) in the experimental density map (Fig. 4c), shows a very low solvent exposure score, whereas the three protruding helices of GDH (Fig. 4b), for which solvent exposure scores are very high, can only be observed as unresolved density at a lower threshold (see Fig. 5).

Additionally, the observed subunit/domain reorientation, which generally leads to an overall compaction of the proteins due to the closing of gaps/cavities, can be related to the solvent exposure score. Morphological features like crevasses ( $\beta$ -Galactosidase), cavities (GroEL), or protruding flexible domains (GDH) result in high solvent exposure scores nearby, which implies that they are strongly affected by dehydration. In these regions, the driving forces to compensate the loss of protein-solvent interactions with intramolecular interactions is large, hence it is likely that reorganisation takes places. When there is a coherent, preferred pathway for domains to reorient, we are able to resolve the final structure, as minimal heterogeneity is introduced into the sample by dehydration; otherwise, we observe a region of lower resolution.

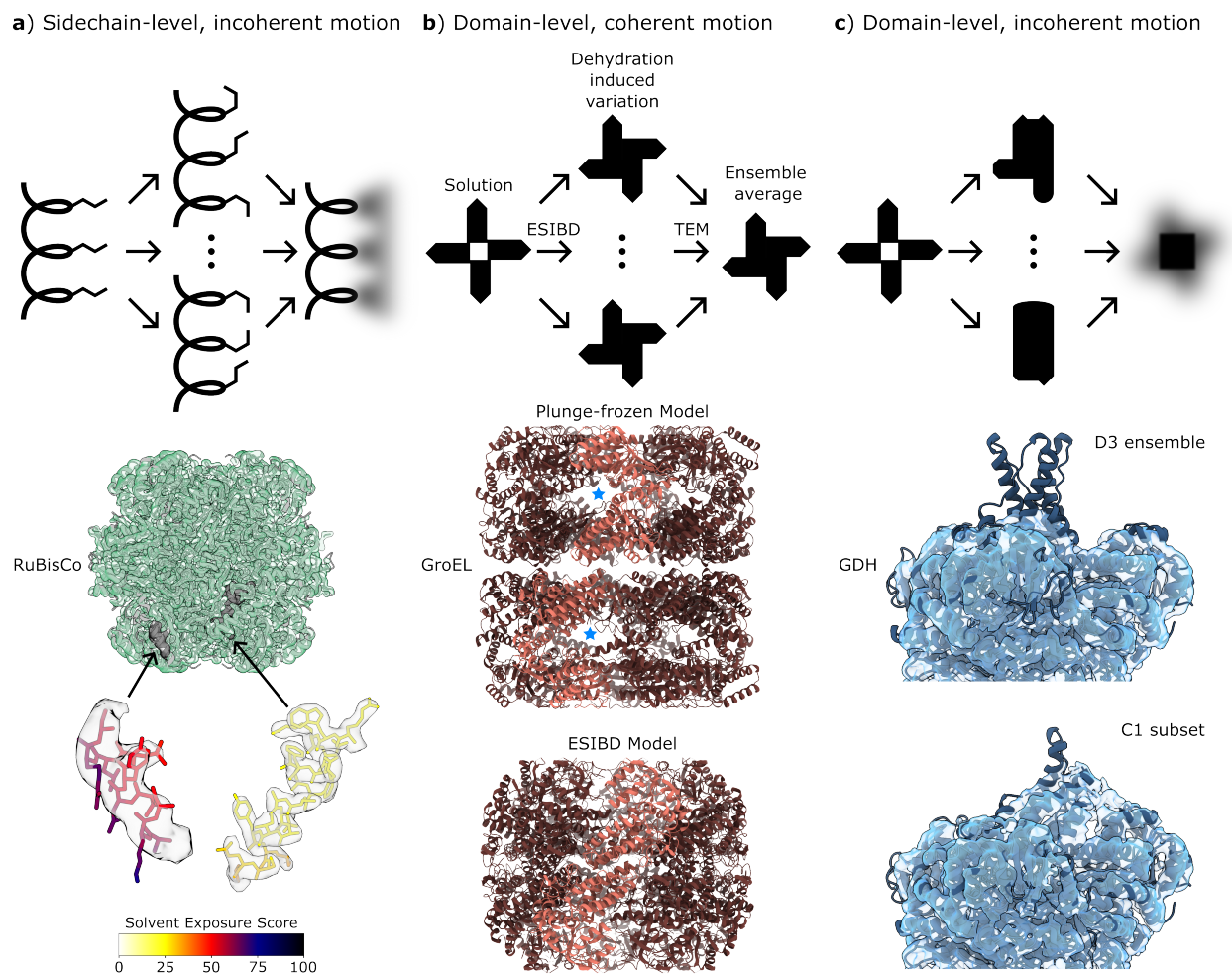


**FIG. 5. Dehydration-induced structural changes in ESIBD-prepared proteins.** **a)** Model of RuBisCo in ESIBD map. Two isolated  $\alpha$ -helices illustrate the dehydration-induced heterogeneity (lack of density) in highly solvent-exposed sidechains. **b)** Comparison between a plunge-frozen GroEL model (PDB entry 5W0S) and the ESIBD-prepared model, with two monomers highlighted to demonstrate the twist and compaction between subunits and blue stars labelling crevices which collapse. **c)** Comparison between consensus D3 map and model and a symmetry-free map and model generated from a subset of particles for GDH, demonstrating the collapse of the three  $\alpha$ -helices which make up an antenna.

For instance, the ESIBD structure of  $\beta$ -Galactosidase shows large parts of the secondary and tertiary structure retained from solution, but dehydration-induced subunit reorientation coherently compacts the protein in the gas phase, in particular closing crevices between  $\beta$ -sheets at the tips of the protein and on the surface of the protein close to the centre (see blue star in Fig. 4a,e).<sup>16</sup>

In comparison, RuBisCo hardly compacts (only 1.5% across its entire width), and its sub-

units reorient less than the other proteins (Fig. 5a). Here, small-scale, incoherent changes are still observed by loss of sidechain resolution in highly solvent-exposed areas of the protein. Two  $\alpha$ -helices are selected as examples, one from the centre of the protein, in which the solvent exposure score is very low for all atoms, and all sidechains are well resolved. In the other helix, taken from the surface of RuBisCo, less solvent-exposed sidechains from the inside of the protein can still be resolved, but the most solvent-exposed sidechains which are on the surface of the protein are entirely unresolved.

The compaction of GroEL is very pronounced, as illustrated by the comparison of a PBD model (5W0S) to our EM map (Fig. 4d,h) or model (Fig. 5b, SI). It undergoes a 24% reduction in height (along the central cavity/C7 axis) but almost no reduction in overall particle width (perpendicular to the C7 axis).<sup>17</sup> This compaction can be clearly seen in Fig. 5b, where we compare a conventional cryoEM model<sup>45</sup> to our model, which was relaxed into our map using ISOLDE and further refined in COOT and Phenix.<sup>46-48</sup> Smaller cavities (shown with blue stars in Fig. 5b) are absent from this map, and the two heptameric rings twist by 5° with respect to each other around the central C7 axis, enabling tighter compaction (see Supplementary Movie S2). This compaction lines up well with collision cross sections previously observed by ion mobility spectrometry, which are lower than expected when computed from plunge-frozen/crystal structures.<sup>49-52</sup>

Finally, GDH has two antennae, made up of one  $\alpha$ -helix per subunit (residues 398 to 425 on PDB model 3JCZ), which are unresolved in the ESIBD map with D3 symmetry imposed. We performed further heterogeneous refinement (shown in detail in Suppl. Fig. S6) with no symmetry applied, yielding a subset of particles which reconstructed a map in which the collapse of one antenna is observed (Fig. 5c). These antennae are the most solvent-exposed region of GDH (see solvent exposure score Fig. 4f) and are known to be flexible.<sup>53,54</sup> Upon transfer into the gas phase, the majority of local interactions are removed, with only the two neighbouring  $\alpha$ -helices offering any stabilising interactions. Consequently, each set of 3  $\alpha$ -helices heterogeneously bends onto the nearby protein surface, forming intramolecular interactions. There is no coherent, preferred pathway for this collapse, leading to a heterogeneous mixture of proteins in the sample. Therefore, cryoEM, while resolving the central domains, struggles to resolve these features.

Generally, for all proteins, rearrangement is driven by the formation of new protein-protein intramolecular interactions if the mechanical properties of the protein permits, i.e., if more energy is gained in the rearrangement than lost due to the straining or breaking of bonds and the weakening of existing intramolecular interactions. These new interaction sites had previously been

occupied by protein-water interactions and become available upon dehydration. We therefore find that domains with an overall high solvent exposure are those which are more strongly involved in rearrangements.

## DISCUSSION

The high-resolution structure determination by cryoEM of several soluble proteins from samples prepared using ESIBD was enabled by providing extensive control of the protein and its environment throughout the entire ESIBD process. To protect the protein structure, we employ gentle native, nano-electrospray in which a combination of low flow rates, low emitter potential, and the presence of small ions to screen electric fields protect the protein structure.<sup>55,56</sup> Native ESI retains the fold of the protein, but once in the gas phase as a dehydrated protein ion, the liquid phase structure which was at thermodynamic equilibrium is no longer the lowest energy configuration. Due to the absence of the solvent, the strength of polar interactions, especially at the protein surface, have increased, while hydrophobic interactions are absent.<sup>44</sup> The structure of the protein is not altered immediately, as it can be in a kinetically trapped state, where any small excitation can overcome barriers towards kinetically accessible rearrangements. If these rearrangements follow the same trajectory, they are coherent (Fig. 5b) we perceive them as domain-level structural changes such as the closing of crevices and cavities in GroEL and  $\beta$ -Galactosidase with only a small loss in resolution. But, in particular at the protein surface, these changes can be random, incoherent motions, which we measure as an increase in heterogeneity and hence in a loss in resolution (Fig. 5c).

We therefore control the ion beam throughout the ESIBD process such that we minimise activation and hence the relaxation of the kinetically trapped solution conformation. To this end, we employ low potential gradients in regions where collisions with neutral gas molecules occur, as ion-gas collisions cannot be avoided. ESI operates at ambient pressure and gentle collisions are needed to thermalise the protein ion beam, which is essential for deposition at low landing energies without loss of intensity. Low energy ion-surface collisions are required to minimise the energy transferred to the protein upon landing, which is especially efficient on freestanding membrane substrates.<sup>57</sup> Finally, we deposit the protein ion onto a substrate at cryogenic temperature to avoid thermally activating structural reorganisation of the adsorbed protein.<sup>14</sup>

The central role of the solvent for the observed structural changes is underpinned by strong correlation of observed structural changes, both random, incoherent reorientations increasing het-

erogeneity and coherent domain movement, with the extent of solvent exposure of that region of the protein. Highly solvent-exposed regions of proteins have a greater thermodynamic drive to rearrange to form intramolecular interactions to replace protein-solvent interactions lost to dehydration. The strength and spatial imbalance of interactions which remain after dehydration are augmented by the absence of electrostatic screening that water provides. These factors, new interactions and those of altered strength, combine to drive rearrangements in solvent-exposed regions which we can identify by the simple tool of the solvent exposure score calculated from a PDB structure. Overall, these structural changes represent a compaction due to dehydration, which we observe for proteins in cryoEM. It provides a microscopic explanation for the observation of protein cross sections being smaller than expected from modelling based on solution structure in ion mobility spectrometry.<sup>49-52</sup>

The growth of a thin film of vitreous ice around deposited proteins by precisely controlling sample temperature during ice growth, the partial pressure of water, and the duration of ice growth has proven essential to the observation of high-resolution structure. Our instrumentation was specifically designed to implement this capability following methodology established in molecular beam epitaxy. Temperature control at the substrate is essential to control the mobility of the adsorbed water molecules: high mobility at high temperature allows for the ordering of water into a poly-crystalline layer, whereas the absence or very low mobility at low temperature leads to the formation of nanostructures.<sup>58</sup> Only precise and long-time stable temperature control allows to find the conditions where diffusion balances with the growth rate such that we obtain amorphous ice which embeds proteins into a flat layer. We speculate that the major effects of the ice layer are improved protection from radiation damage and re-introduction of some polar and van der Waals interactions that had been lost upon dehydration. While at low temperature the protein cannot relax its structure on domain level, the mobility on the level of the individual water molecule—evidenced by the fabrication of a smooth layer—will allow also for small rearrangements, in particular at the protein's surface where dehydration has the greatest effect. As a consequence we observe improvement over ice-free cryoEM imaging in terms of resolution.<sup>33</sup>

An advantage of ESIBD is maintaining the purity and integrity of the sample throughout the entire process. UHV conditions in the deposition stage, shielding of the sample from exposure to warm, particle-emitting surfaces, as well as an elaborate sample transfer through a water-free nitrogen environment are employed to minimise the contamination while maintaining sample temperature. Mass selection ensures chemical purity and increases homogeneity. The removal of

complexes with incorrect or undesired stoichiometry (see Fig. 3) and other solution contamination greatly aids the efficiency of particle picking and adds confidence in the obtained class averages even at lower resolution because chemically pure samples are imaged. In addition,  $m/z$  filtering enables chemical selectivity that promises additional features, such as the gas-phase enrichment of low abundance species for structural investigation, for instance complexes of special stoichiometry<sup>59,60</sup> or protein-ligand interactions.<sup>11,61</sup>

Based on the success of these studies on soluble proteins, we are extending the ESIBD for cryoEM approach further by investigating the gas-phase structure of membrane proteins.<sup>62–64</sup> Like for protein-ligand interactions, it will be essential to control the interactions and the environment of the proteins to protect their structure and allow for high resolution imaging. Finally, together with the recent achievements of laser flash melting in restoring native protein structure after ESIBD,<sup>17,65</sup> the preparation of protein samples through mass selected vacuum deposition has the potential to become feasible for applications in structural biology.

## METHODS

### *Solution Preparation*

GDH (G7882) was purchased from Sigma-Aldrich; the lyophilised powder was reconstituted in 200 mM ammonium acetate (pH 6.9) to a final concentration of 20  $\mu$ M.  $\beta$ -Galactosidase<sup>16</sup> and GroEL<sup>33</sup> were prepared as previously described.

RuBisCo was prepared using established methods.<sup>66</sup> Briefly, *Arabidopsis thaliana* seedlings were grown on Murashige and Skoog medium plates (0.65% agar) to 14d, then macerated in chloroplast isolation buffer (CIB; 0.3 M sorbitol, 20 mM HEPES-KOH pH 8.0, 10 mM NaHCO<sub>3</sub>, 5 mM MgCl<sub>2</sub>, 5 mM EDTA, 5 mM EGTA). Macerated cells were filtered through two layers of Miracloth (Merck, Darmstadt) and pelleted for 5 minutes at 1000 x g. Cell pellets were re-suspended in CIB buffer and layered over a preprepared 50% percoll (Cytiva, Uppsala) in CIB gradient. Broken and whole chloroplasts were separated by density gradient centrifugation for 10 minutes at 7800 x g. Whole chloroplasts were washed in HMS buffer (0.3 M sorbitol, 50 mM HEPES-NaOH pH 8.0, 3 mM MgSO<sub>4</sub>), then lysed for 1 hour in hypotonic lysis buffer (25 mM HEPES-KOH pH 8.0 with protease inhibitor). The stroma of lysed chloroplasts was obtained by laying lysed chloroplasts over the 0.3 M MOPS (0.3 M sucrose, 10 mM MOPS pH 7.8, 4

mM MgCl<sub>2</sub>) step of a sucrose step gradient and centrifuged at 80000 x g to separate soluble and membrane fractions. Large complexes were concentrated using a 100000 Da molecular weight concentrator.

All proteins were desalted by eluting through two P6 buffer exchange columns (7326222, Bio-Rad), equilibrated with 200 mM ammonium acetate (pH 6.9). They were then diluted in 200 mM ammonium acetate (pH 6.9) to reach the concentration used for native MS: 10  $\mu$ M ( $\beta$ -Galactosidase and GDH), 5 mg / mL (RuBisCo), and 5  $\mu$ M (GroEL). Buffer exchange was always done on the day of deposition.

### *Native MS*

Native MS was performed as previously described.<sup>33</sup>

### *Preparation of ESIBD cryoEM samples*

Mesh size 400 copper TEM grids with 3 nm amorphous carbon on a lacey carbon film (AGS187-4) were purchased from Agar Scientific and gold TEM grids with mesh size 300 and 2 nm amorphous carbon on a R1.2/1.3 holey gold film (C2-A14nAu30-50) were purchased from Quantifoil.

Grids were clipped into autogrid carriers then plasma cleaned for 30 seconds before deposition. The clipped, cleaned grid was loaded into the cryoshuttle, where it is held in position by springs. The top was then closed, isolating the grid from the atmosphere during transfer. The shuttle was loaded partially into the stage before deposition, to achieve good thermal contact, but the grid is not yet exposed to atmosphere to keep the grid cleaner when ice is already condensed on the stage, as insertion of the room temperature cryoshuttle heats up the stage, sublimating some water. After 5 minutes of temperature equilibration, the cryoshuttle was fully inserted and ready for deposition with the grid exposed.

Deposition methodology is described in the workflow section above, and transfer into liquid nitrogen is performed as previously described.<sup>16</sup>

## ***Movie acquisition and processing***

All micrographs were collected using a Thermo Scientific Krios 300 kV cryo-TEM equipped with a BioQuantum energy filter operated at a slit width of 20 eV and a K3 direct electron detector (both Gatan), located at the COSMIC cryoEM facility. Automated data acquisition was controlled using EPU software (Thermo Scientific). All movies were recorded in the tif format, using a range of defocus settings between -1 and -3  $\mu\text{m}$ , an exposure of  $40 e^-/\text{\AA}^2$ , and a magnification of 105,000 corresponding to a pixel size of 0.83  $\text{\AA}$ .

Data were processed using cryoSPARC.<sup>42</sup> After running Patch Motion Corr. and Patch CTF jobs, particles were picked using template picking, based on templates from manual picking, and extracted. After multiple rounds of 2D and 3D classification, final maps were produced using local refinement ( $\beta$ -Galactosidase, GDH, RuBisCo) or non-uniform refinement (GroEL), based on ab initio initial volumes generated from our data. This was followed by local resolution estimation. Symmetry was imposed in non-uniform refinement and local refinement, but using C1 symmetry resulted in only slightly lower resolution. Figures and movies of the resulting 3D EM density maps were generated using ChimeraX.<sup>67</sup> Further movie acquisition and processing details are specified in figs. S3 to S6 and table S2.

## ***Solvent Exposure Score***

Using a python script, the solvent exposure score is calculated for each non-hydrogenic atom,  $i$ , in the plunge-frozen structure of the proteins ( $\beta$ -Galactosidase: 6CVM; GDH: 3JCZ; RuBisCo: provided by J. Bolla; GroEL: 5W0S). We sum up the  $m_j d_{ij}^{-2}$  where  $d_{ij}$  is the distance (measured in  $\text{\AA}$ ) between the atom  $i$  and all other atoms  $j$  (with atomic mass  $m_j$ ) for all atoms within 50  $\text{\AA}$  which are not covalently bound to atom  $i$  ( $1.85 \text{\AA} < d_{ij} < 50 \text{\AA}$ ). We then subtract the resulting score from a maximal score (404.3) obtained from all proteins considered with water modelled in, and then divide by the maximal score to normalise the final score on a scale from 0 to 100 (though negative values are, in principle, possible). This yields a score which represents solvent-exposed parts with a high value and concealed parts with a low value. This is visualised in ChimeraX by colouring the protein by the calculated scores; when we display the proteins in cartoon view, we averaged the scores of each atom within each residue to choose the displayed score for said residue. The plots and atomic models still display all atoms, without averaged scores. Code is

available at [https://github.com/lukasaerik/solvent\\_exposure](https://github.com/lukasaerik/solvent_exposure)

### ***Tomogram acquisition and processing***

Tomographic data were acquired with the Titan Krios described above. Tilt series were collected with SerialEM<sup>68</sup> using dose-symmetric acquisition ( $\pm 60^\circ$ ) with  $3^\circ$  tilt increments at a magnification of 81000 and pixel size of 1.106 Å/pixel. Image frames (0.24 s exposure/frame) were collected at a dose rate of 11.3 e-/pixel/s at a target defocus of -4  $\mu\text{m}$ . Tomograms were reconstructed using IMOD.<sup>69</sup>

### ***Preparation of ESIBD STM samples***

Single crystals of gold and copper were obtained from MaTeck GmbH, with the (111) and (100) faces polished, respectively. To achieve a clean, atomically-flat surface, 3 cycles of sputtering (Ar,  $p = 10^{-5}$  mbar, 1 kV DC electron gun) and annealing (with resistive heater, to 800 K for 5 mins) were used. Samples were then transferred into a UHV vacuum suitcase,<sup>70</sup> removed from the SPM by venting the loadlock, and carried to the ESIBD instrument; the loadlock was pumped to  $2 \times 10^{-8}$  mbar, and the sample was transferred into the deposition stage.

$\beta$ -Cyclodextrin (C4767), purchased from Sigma Aldrich, was dissolved into a 50:50 v:v solution of deionised water (MilliQ):HPLC grade methanol to yield a final concentration of 10  $\mu\text{M}$ . Bovine serum albumin (A0281) was purchased from Sigma Aldrich, then 9 mg were dissolved into 24.75 mL deionised (MilliQ) water, 24.75 mL HPLC grade acetonitrile, and 0.5 mL HPLC grade formic acid. The plasmid pUC19 (SD0061), in a 10 mM Tris-HCl and 1 mM EDTA buffer, was purchased from Thermo Scientific. This was then diluted in a solution of 66% v/v ACN (in deionised (MilliQ) water) to a final plasmid concentration of 0.3 nM.

Solution was added to gold-coated (with a sputter coater: 108A/SE, Cressington) nano-ESI emitters pulled from borosilicate glass capillaries (30-0042, Harvard Bioscience) using a pipette puller (P-1000, Sutter Instrument). Normal MS setting were used, with lower HCD cell pressure for thermalising the ion beam. First, a mass spectrum without mass selection was obtained, and then mass selection was used to isolate and deposit only the desired species. For  $\beta$ -cyclodextrin, individual adducts (specifically just the  $\text{Na}^+$  adduct) were selected for deposition. Sample potential was set to -9 V for a landing energy of 2 eV per charge. Charge accumulated was monitored

to measure the amount of ions deposited: 2 pAh for  $\beta$ -cyclodextrin, 16 pAh for bovine serum albumin, and 10 pAh for pUC19.

After deposition, the sample was transferred into the vacuum suitcase, the loadlock was vented, the suitcase was carried to the SPM, and the loadlock on the SPM was pumped to  $2 \times 10^{-8}$  mbar. The sample was then transferred into the microscope head, allowed to stabilise in temperature (9.3 to 9.7 K). Samples were imaged using scanning tunnelling microscopy in constant current mode with tunnelling currents between 1 and 100 pA and images were processed in Gwyddion.<sup>71</sup>

## ACKNOWLEDGMENTS

We wish to acknowledge support from Thermo Fisher Scientific who provided the Q Exactive UHMR mass spectrometer and the Aquilos sample transfer system within the framework of a technology alliance partnership. We thank E. Silvester for her help with tomogram acquisition. We wish to acknowledge support from the COSMIC microscope facility, especially from R. Matadeen.

## Funding

This research was supported by the BBSRC (BB/W017024/1, BB/V019694/1) and the EPSRC (EP/V051474/1). L.T.S. is funded by the Wellcome Trust (218482/Z/19/Z; Wellcome-funded 4 year PhD program in Cellular Structural Biology). Research in the J.R.B. laboratory is supported by the Royal Society through the University Research Fellowship grant (URF/R1/211567). L.E. acknowledges DPhil funding from Vertex Pharmaceuticals.

## Author Contributions

L.E., T.K.E., and S.R. conceived the experiments. L.E., T.K.E., P.F., and S.R. designed and constructed the custom deposition hardware. T.R. and J.R.B. expressed and purified RuBisCo. L.E., T.K.E., and S.B.K. prepared solutions, performed native ESIBD, imaged, and performed data analysis for cryoEM samples. L.T.S. and L.B. collected and built all tomography data. L.E. and M.G. prepared solutions, performed ESIBD, and imaged STM samples. L.E. and S.R. drafted the manuscript. All authors contributed to the interpretation of results and reviewed the manuscript.

## **Competing Interests**

T.K.E. is an employee of Thermo Fisher Scientific, manufacturer of the Q Exactive UHMR, Aquilos, Arctica, and Krios instruments used in this research.

## **Data Availability Statement**

cryoEM maps are available in the Electron Microscopy Data Bank (EMDB) under the following accession codes: EMD-57226 ( $\beta$ -Galactosidase), EMD-57223 (GDH; D3), EMD-57224 (GDH; C1 Subset), EMD-57225 (RuBisCo), and EMD-52626 (GroEL). Models are available in the RCSB Protein Data Bank (PDB) under the following accession codes: 29KD ( $\beta$ -Galactosidase), 29KB (GDH), 29KC (RuBisCo), and 29KA (GroEL).

**Supplementary Materials for  
High-resolution cryoEM structure determination of soluble proteins after  
soft-landing ESIBD.**

Lukas Eriksson *et al.*

Corresponding Author: stephan.rauschenbach@chem.ox.ac.uk

**This PDF file includes**

Figures S1 to S6

Tables S1 and S2

Equations S1 and S2

**Other Supplementary Materials for this manuscript include the following:**

Movies S1 and S2

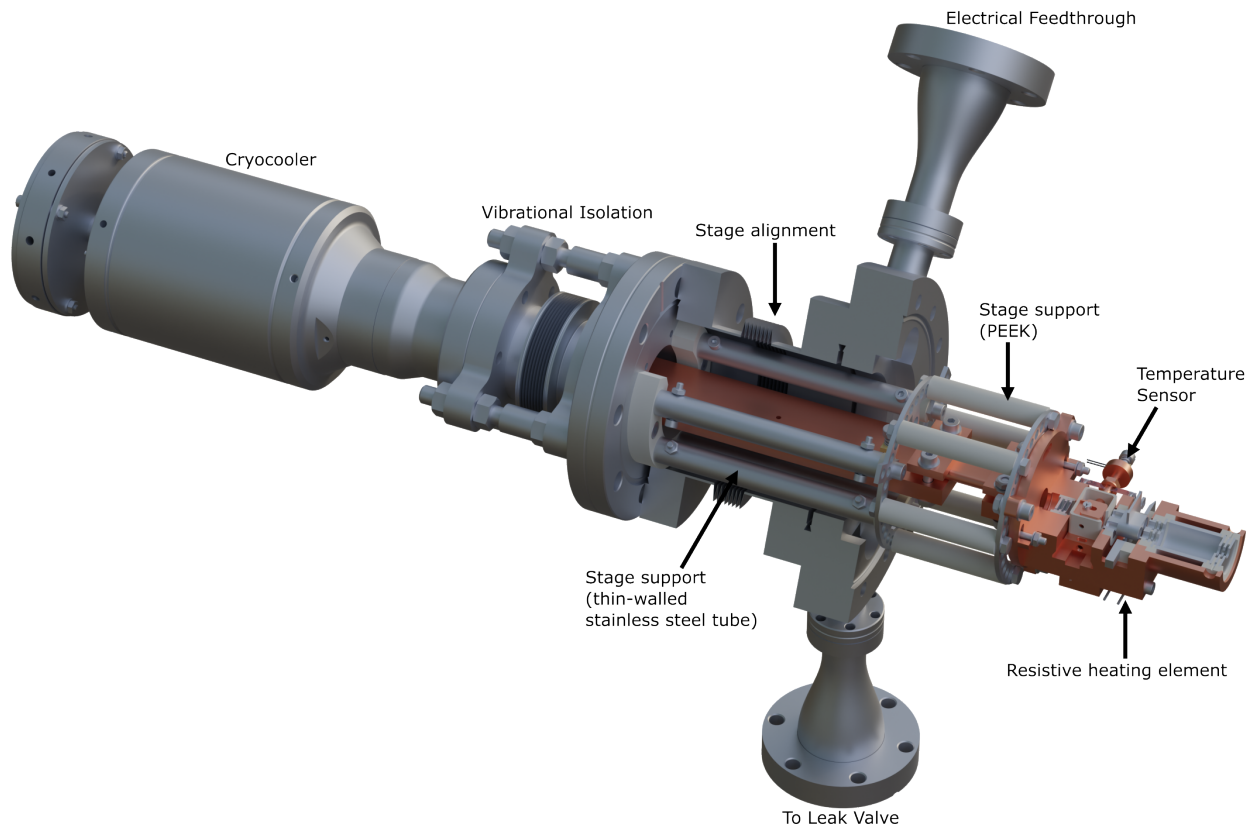
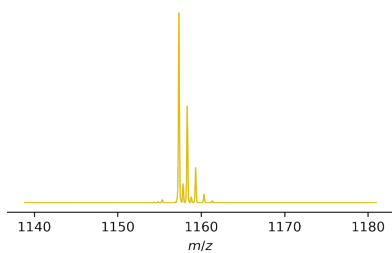
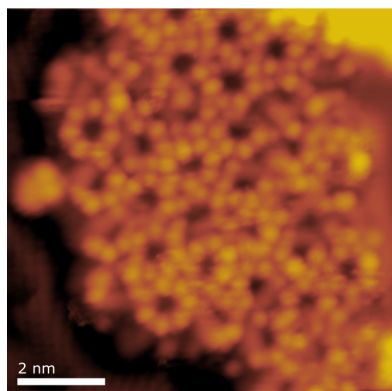


FIG. Fig. S1. **Deposition stage, support, and cryocooler** shown in half-section view of mounting flange. Key components are labelled.

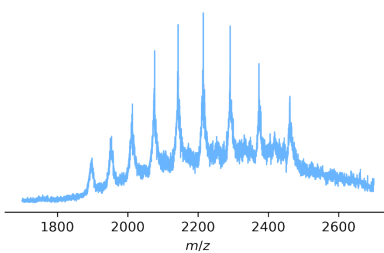
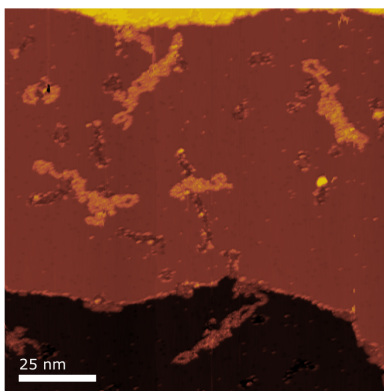
SPM samples are transferred under continuous UHV conditions to the microscope, relying on loadlocks, which reach below  $2 \times 10^{-8}$  mbar within an hour of pumping, and a UHV suitcase, which remains below  $10^{-10}$  mbar. Three classes of molecules were deposited for proof-of-principle scanning tunneling microscopy (STM) experiments:  $\beta$ -cyclodextrin, a 1135 Da cyclic oligosaccharide; bovine serum albumin (BSA), a 66 kDa protein; and pUC19, a 1.7 MDa plasmid; representative micrographs are shown in Supplementary Figure S2. A new suitcase is in development to allow for the fully cryogenic transfer of samples.

$$15 \times 10^{-12} Ah \times \frac{3600s}{1h} \times \frac{1z}{1.602176634 \times 10^{-19}C} \times \frac{1 \text{ GDH}}{36z} \approx 9.4 \times 10^9 \text{ GDH molecules} \quad (1)$$

$$10^{10} \text{ GDH molecules} \times \frac{10^{-5} \text{ mm} \times 10^{-5} \text{ mm}}{1 \text{ GDH molecule}} \div 4 \text{ mm}^2 \approx 25\% \text{ of monolayer coverage} \quad (2)$$

a)  $\beta$ -Cyclodextrin

b) Denatured BSA



c) pUC19 Plasmid

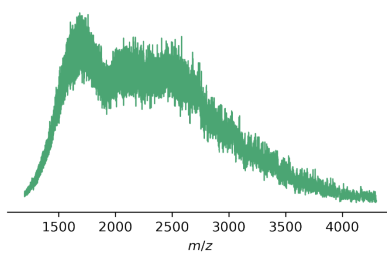
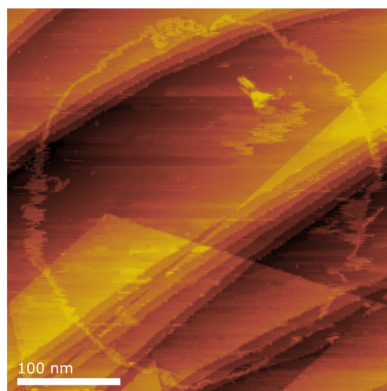


FIG. Fig. S2. **ESIBD-prepared STM samples.** Representative micrographs and deposited mass spectra for (a)  $\beta$ -cyclodextrin on Au(111), b) denatured bovine serum albumin on Cu(100), and c) pUC19, a plasmid, on Au(111).

TABLE Table S1. **CryoEM data collection settings for ice micrographs and cryoET.**

	Ice Micrographs	CryoET
<b>Data collection</b>		
Microscope	Talos Arctica	Krios G3
Magnification	105,000	81,800
Voltage (kV)	200	300
Electron exposure ( $e^-/\text{\AA}^2$ )	40	2.22 per frame (90.9 total)
Defocus ( $\mu\text{m}$ )	-3	-4
Pixel size ( $\text{\AA}$ )	1.17	1.106

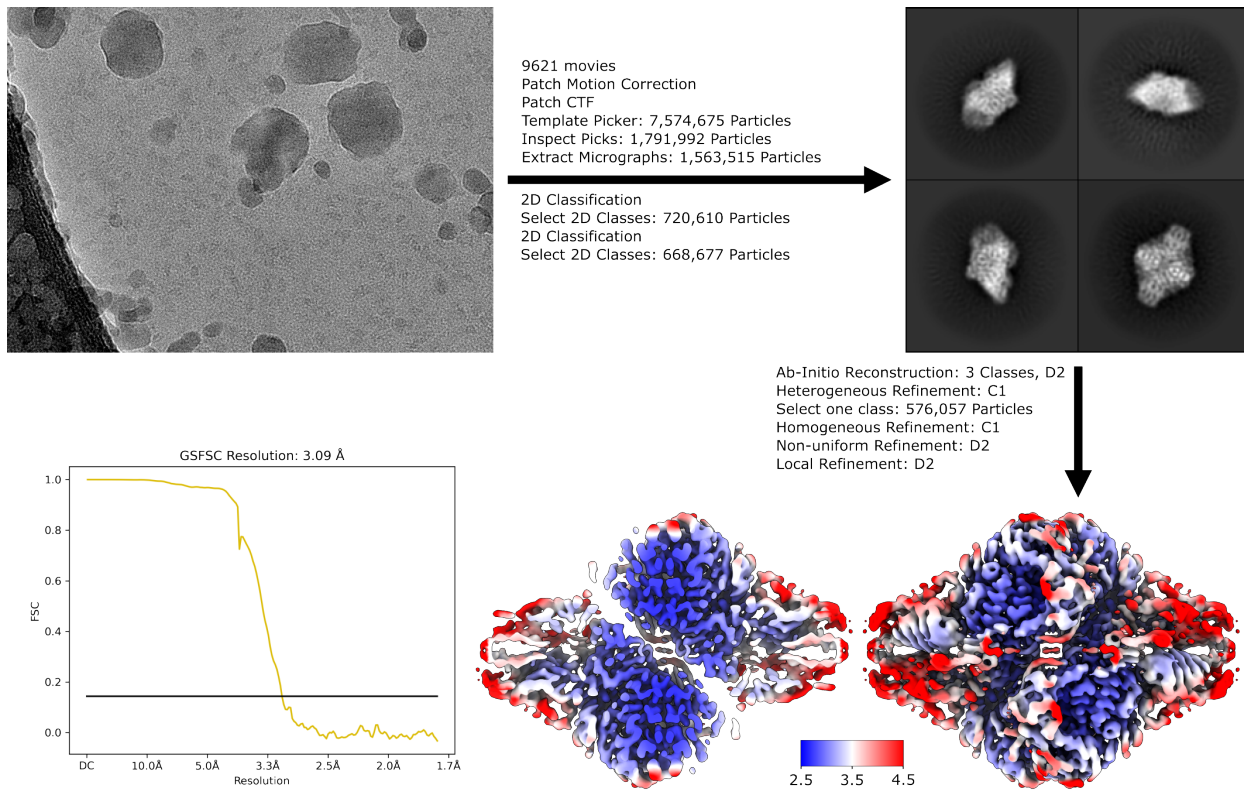


FIG. Fig. S3.  $\beta$ -galactosidase processing pipeline and local resolution map.

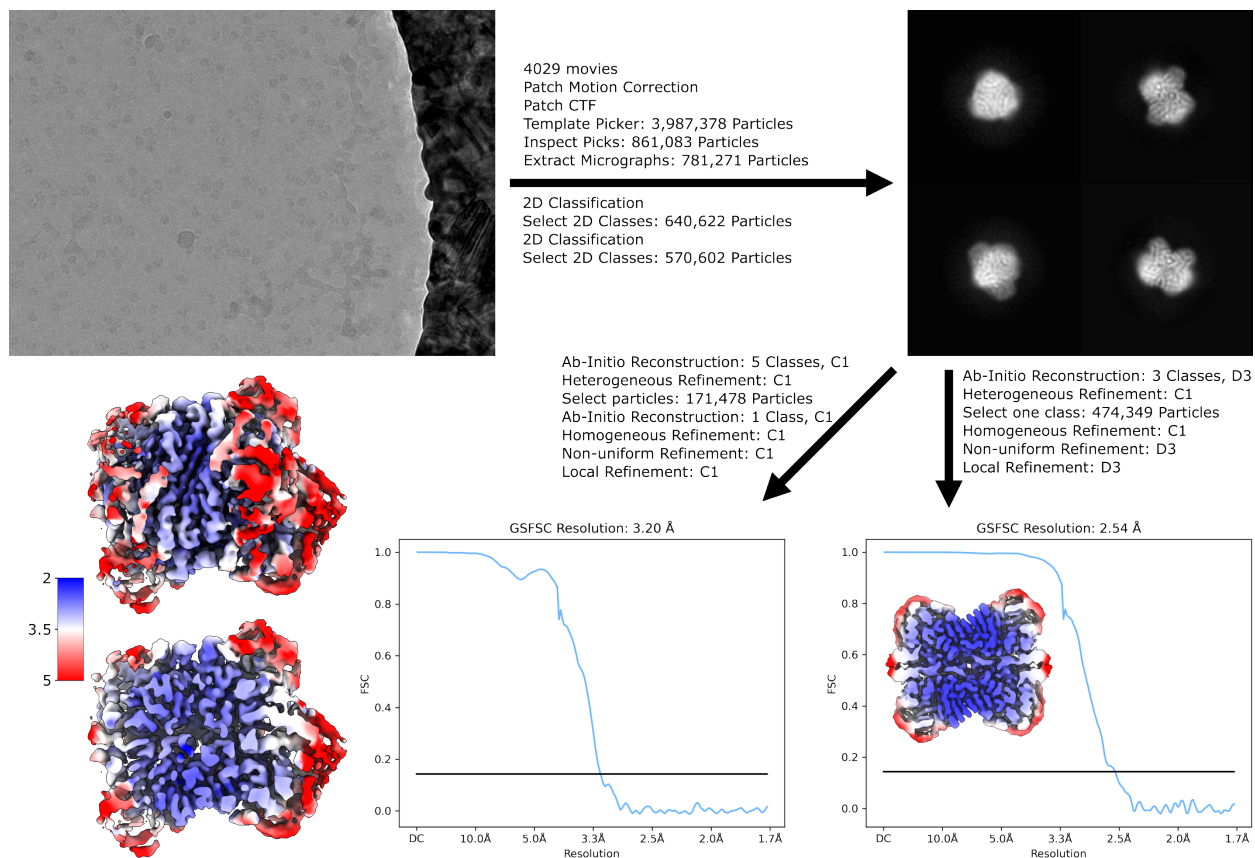


FIG. Fig. S4. **Glutamate Dehydrogenase (GDH) processing pipeline and local resolution map of C1 subset.**

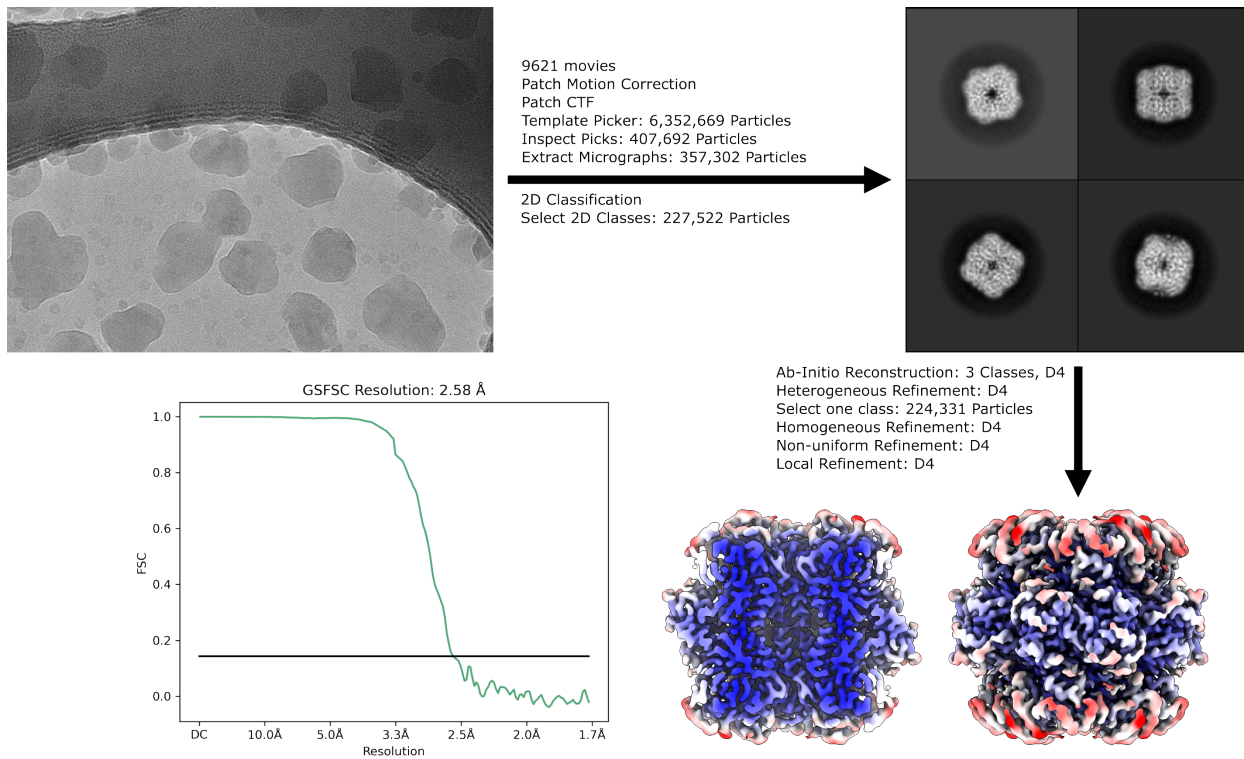


FIG. Fig. S5. RuBisCo processing pipeline.

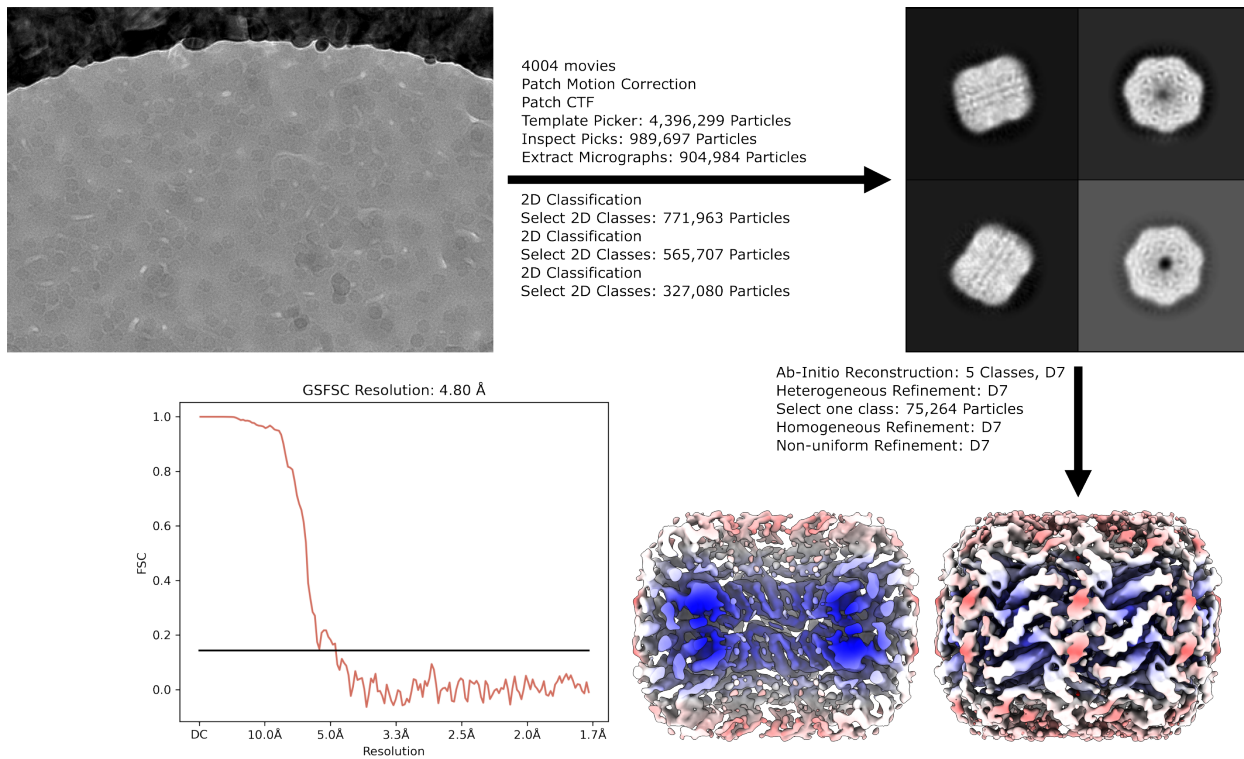


FIG. Fig. S6. GroEL processing pipeline.

TABLE Table S2. Cryo-EM data collection, refinement, and validation statistics.

	$\beta$ -galactosidase	GDH	GDH (C1)	RuBisCo	GroEL
	EMD-57226	EMD-57223	EMD-57224	EMD-57225	EMD-52626
	PDB: 29KD	PDB: 29KB		PDB: 29KC	PDB: 29KA
<b>Data collection and processing</b>					
Microscope	Krios G3	Krios G3	Krios G3	Krios G3	Krios G3
Magnification	105,000	105,000	105,000	105,000	105,000
Voltage (kV)	300	300	300	300	300
Electron exposure ( $e^-/\text{\AA}^2$ )	40	40	40	40	40
Defocus range ( $\mu\text{m}$ )	-1.5 to -3	-1 to -2.5	-1 to -2.5	-1.5 to -3	-1 to -2.5
Pixel size ( $\text{\AA}$ )	0.83	0.83	0.83	0.83	0.83
Symmetry imposed	D2	D3	C1	D4	D7
Initial particle images (no.)	668,677	570,602	570,602	227,522	327,080
Final particle images (no.)	576,057	474,349	171,478	224,331	75,264
Map resolution ( $\text{\AA}$ )	3.09	2.54	3.20	2.58	4.80
FSC threshold	0.143	0.143	0.143	0.143	0.143
Map resolution range ( $\text{\AA}$ , FSC 0.143)	1.9 to 4.5	1.8 to 5.3	2.0 to 6.0	1.8 to 3.4	3.2 to 6.5
FSC 0.5	2.58 to 5.1	2.25 to 5.8	2.7 to 6.8	2.3 to 4.1	4.45 to 8.4
<b>Refinement</b>			N/A		
Initial model used (PDB code)	6CVM	3JCZ		N/A	5W0S
Model resolution ( $\text{\AA}$ )	3.0/3.1/3.3	2.5/2.5/18.5		2.5/2.6/2.7	4.6/4.7/24.5
FSC threshold	0/0.143/0.5	0/0.143/0.5		0/0.143/0.5	0/0.143/0.5
Map sharpening B factor ( $\text{\AA}^2$ )	-151.5	-110.1	-92.5	-109.2	-399.6
Model composition					
Non-hydrogen atoms	22208	14622		31896	23030
Protein residues	3520	2262		4472	4690
Ligands	0	0		0	0
R.m.s. deviations					
Bond lengths ( $\text{\AA}$ )	0.006	0.003		0.003	0.003
Bond angles ( $^\circ$ )	0.772	0.561		0.673	0.535
Validation					
MolProbity score	2.24	1.79		2.04	1.32
Clashscore	5	5		6	1
Poor rotamers (%)	3.1	2.2		1.8	N/A
Ramachandran plot					
Favored (%)	90	96		92	90
Allowed (%)	10	4		8	9
Disallowed (%)	0	0.3		0.3	0.5

**Movie S1:** Animation of the a TEM grid being loaded in the cryoshuttle and subsequent exposure.

**Movie S2:** Morph between solution (5W0S) and ESIBD models of GroEL.

## REFERENCES

- <sup>1</sup>I. Liko, T. M. Allison, J. T. S. Hopper, and C. V. Robinson, “Mass spectrometry guided structural biology,” *Current Opinion in Structural Biology* **40**, 136–144 (2016).
- <sup>2</sup>H. M. Britt and C. V. Robinson, “Traversing the drug discovery landscape using native mass spectrometry,” *Current Opinion in Structural Biology* **91**, 102993 (2025).
- <sup>3</sup>A. J. R. Heck, “Native mass spectrometry: a bridge between interactomics and structural biology,” *Nature methods* **5**, 927–33 (2008).
- <sup>4</sup>S. Tamara, M. A. den Boer, and A. J. R. Heck, “High-resolution native mass spectrometry,” *Chemical Reviews* **122**, 7269–7326 (2022).
- <sup>5</sup>Y. Cheng, N. Grigorieff, P. Penczek, and T. Walz, “A primer to single-particle cryo-electron microscopy,” *Cell* **161**, 438–449 (2015).
- <sup>6</sup>E. Callaway, “Revolutionary cryo-em is taking over structural biology,” *Nature* **201**, 527 (2020).
- <sup>7</sup>J. Gault, I. Liko, M. Landreh, D. Shutin, J. R. Bolla, D. Jefferies, M. Agasid, H.-Y. Yen, M. J. G. W. Ladds, D. P. Lane, S. Khalid, C. Mullen, P. M. Remes, R. Huguet, G. McAlister, M. Goodwin, R. Viner, J. E. P. Syka, and C. V. Robinson, “Combining native and ‘omics’ mass spectrometry to identify endogenous ligands bound to membrane proteins,” *Nature Methods* **17**, 505–508 (2020).
- <sup>8</sup>E. Christofi and P. Barran, “Ion mobility mass spectrometry (im-ms) for structural biology: Insights gained by measuring mass, charge, and collision cross section,” *Chem. Rev.* **123**, 2902–2949 (2023).
- <sup>9</sup>S. A. Chandler and J. L. P. Benesch, “Mass spectrometry beyond the native state,” *Current Opinion in Chemical Biology* **42**, 130–137 (2018).
- <sup>10</sup>S. Rauschenbach, M. Ternes, L. Harnau, and K. Kern, “Mass spectrometry as a preparative tool for the surface science of large molecules,” *Annu Rev Anal Chem (Palo Alto Calif)* **9**, 473–98 (2016).
- <sup>11</sup>X. Wu, M. Delbianco, K. Anggara, T. Michnowicz, A. Pardo-Vargas, P. Bharate, S. Sen, M. Pristl, S. Rauschenbach, U. Schlickum, S. Abb, P. H. Seeberger, and K. Kern, “Imaging single glycans,” *Nature* **582**, 375–378 (2020).
- <sup>12</sup>K. Anggara, L. Sršan, T. Jaroentomechai, X. Wu, S. Rauschenbach, Y. Narimatsu, H. Clausen, T. Ziegler, R. L. Miller, and K. Kern, “Direct observation of glycans bonded to proteins and lipids at the single-molecule level,” *Science* **382**, 219–223 (2023).

- <sup>13</sup>N. Vats, S. Rauschenbach, W. Sigle, S. Sen, S. Abb, A. Portz, M. Dürr, M. Burghard, P. A. van Aken, and K. Kern, “Electron microscopy of polyoxometalate ions on graphene by electrospray ion beam deposition,” *Nanoscale* **10**, 4952–4961 (2018).
- <sup>14</sup>T. K. Esser, J. Böhning, P. Fremdling, T. Bharat, J. Gault, and S. Rauschenbach, “Cryo-em samples of gas-phase purified protein assemblies using native electrospray ion-beam deposition,” *Faraday Discuss.* **240**, 67–80 (2022).
- <sup>15</sup>P. Fremdling, T. K. Esser, B. Saha, A. A. Makarov, K. L. Fort, M. Reinhardt-Szyba, J. Gault, and S. Rauschenbach, “A preparative mass spectrometer to deposit intact large native protein complexes,” *ACS Nano* **16**, 14443–14455 (2022).
- <sup>16</sup>T. K. Esser, J. Böhning, A. Önür, D. K. Chinthapalli, L. Eriksson, M. Grabarics, P. Fremdling, A. Konijnenberg, A. Makarov, A. Botman, C. Peter, J. L. P. Benesch, C. V. Robinson, J. Gault, L. Baker, T. A. M. Bharat, and S. Rauschenbach, “Cryo-em of soft-landed  $\beta$ -galactosidase: Gas-phase and native structures are remarkably similar,” *Science Advances* **10**, eadl4628 (2024).
- <sup>17</sup>S. V. Barrass, T. K. Esser, N. J. Mowry, L. Eriksson, J. Hruby, L. T. Seeley, W. A. Curtis, L. A. Baker, M. Drabbels, S. Rauschenbach, and U. J. Lorenz, “Cryo-em sample preparation with soft-landing and laser flash melting,” *bioRxiv*, 2025.06.05.657968 (2025).
- <sup>18</sup>A. Walz, K. Stoiber, A. Huettig, H. Schlichting, and J. V. Barth, “Navigate flying molecular elephants safely to the ground: Mass-selective soft landing up to the mega-dalton range by electrospray controlled ion-beam deposition,” *Analytical Chemistry* **94**, 7767–7778 (2022), doi: 10.1021/acs.analchem.1c04495.
- <sup>19</sup>G. E. Johnson, Q. Hu, and J. Laskin, “Soft landing of complex molecules on surfaces.” *Annual review of analytical chemistry (Palo Alto, Calif.)* **4**, 83–104 (2011).
- <sup>20</sup>M. S. Westphall, K. W. Lee, A. Z. Salome, J. M. Lodge, T. Grant, and J. J. Coon, “Three-dimensional structure determination of protein complexes using matrix-landing mass spectrometry,” *Nature Communications* **13**, 2276 (2022).
- <sup>21</sup>C. Hamann, R. Woltmann, I.-P. Hong, N. Hauptmann, S. Karan, and R. Berndt, “Ultrahigh vacuum deposition of organic molecules by electrospray ionization,” *Review of Scientific Instruments* **82** (2011).
- <sup>22</sup>H. Y. Samayoa-Oviedo, K.-A. Behrend, S. Kawa, H. Knorke, P. Su, M. E. Belov, G. Anderson, J. Warneke, and J. Laskin, “Design and performance of a soft-landing instrument for fragment ion deposition,” *Anal. Chem.* **93**, 14489–14496 (2021).
- <sup>23</sup>V. Franchetti, B. H. Solka, W. E. Baitinger, J. W. Amy, and R. G. Cooks, “Soft landing of ions

- as a means of surface modification,” *International Journal of Mass Spectrometry and Ion Physics* **23**, 29–35 (1977).
- <sup>24</sup>M. S. Westphall, K. W. Lee, C. Hemme, A. Z. Salome, K. Mertz, T. Grant, and J. J. Coon, “Cryogenic soft landing improves structural preservation of protein complexes,” *Anal. Chem.* **95**, 15094–15101 (2023).
- <sup>25</sup>W. G. Baechler, “Cryopumps for research and industry,” *Vacuum* **37**, 21–29 (1987).
- <sup>26</sup>S. Tacke, P. Erdmann, Z. Wang, S. Klumpe, M. Grange, J. Plitzko, and S. Raunser, “A streamlined workflow for automated cryo focused ion beam milling,” *Journal of Structural Biology* **213**, 107743 (2021).
- <sup>27</sup>S. Abb, L. Harnau, R. Gutzler, S. Rauschenbach, and K. Kern, “Two-dimensional honeycomb network through sequence-controlled self-assembly of oligopeptides,” *Nature Communications* **7**, 10335 (2016).
- <sup>28</sup>R. S. Smith, Z. Dohnálek, G. A. Kimmel, K. P. Stevenson, and B. D. Kay, “The self-diffusivity of amorphous solid water near 150 k,” *Chemical Physics* **258**, 291–305 (2000).
- <sup>29</sup>C. He, W. Zhang, and Y. Li, “The glass transition behaviors of low-density amorphous ice films with different thicknesses,” *J. Chem. Phys.* **133**, 204504 (2010).
- <sup>30</sup>O. Mishima and H. E. Stanley, “The relationship between liquid, supercooled and glassy water,” *Nature* **396**, 329–335 (1998).
- <sup>31</sup>L. A. Passmore, C. J. Russo, and R. A. Crowther, “Chapter three - specimen preparation for high-resolution cryo-em,” in *Methods in Enzymology*, Vol. 579 (Academic Press, 2016) pp. 51–86.
- <sup>32</sup>G. Weissenberger, R. J. M. Henderikx, and P. J. Peters, “Understanding the invisible hands of sample preparation for cryo-em,” *Nature Methods* **18**, 463–471 (2021).
- <sup>33</sup>T. K. Esser, J. Böhning, P. Fremdling, M. T. Agasid, A. Costin, K. Fort, A. Konijnenberg, J. D. Gilbert, A. Bahm, A. Makarov, C. V. Robinson, J. L. P. Benesch, L. Baker, T. A. M. Bharat, J. Gault, S. Rauschenbach, and J. Wand, “Mass-selective and ice-free electron cryomicroscopy protein sample preparation via native electrospray ion-beam deposition,” *PNAS Nexus* **1** (2022).
- <sup>34</sup>J. Dubochet, M. Adrian, J. J. Chang, J. C. Homo, J. Lepault, A. W. McDowell, and P. Schultz, “Cryo-electron microscopy of vitrified specimens.” *Quarterly reviews of biophysics* **21**, 129–228 (1988).
- <sup>35</sup>A. G. Dirks and H. J. Leamy, “Columnar microstructure in vapor-deposited thin films,” *Thin Solid Films* **47**, 219–233 (1977).

- <sup>36</sup>M. Lee, S. Y. Lee, M.-H. Kang, T. K. Won, S. Kang, J. Kim, J. Park, and D. J. Ahn, “Observing growth and interfacial dynamics of nanocrystalline ice in thin amorphous ice films,” *Nature Communications* **15**, 908 (2024).
- <sup>37</sup>H. Shi, C. Wu, and X. Zhang, “Addressing compressive deformation of proteins embedded in crystalline ice,” *Structure* **31**, 213–220.e3 (2023).
- <sup>38</sup>L. Bernier, H. Pinfeld, M. Pauly, S. Rauschenbach, and J. Reiss, “Gas flow and ion transfer in heated esi capillary interfaces,” *J. Am. Soc. Mass Spectrom.* **29**, 761–773 (2018).
- <sup>39</sup>L. Bernier, M. Taesch, S. Rauschenbach, and J. Reiss, “Transfer conditions and transmission bias in capillaries of vacuum interfaces,” *International Journal of Mass Spectrometry* **447**, 116239 (2020).
- <sup>40</sup>J. P. McGee, R. D. Melani, P. F. Yip, M. W. Senko, P. D. Compton, J. O. Kafader, and N. L. Kelleher, “Isotopic resolution of protein complexes up to 466 kda using individual ion mass spectrometry,” *Analytical chemistry* **93**, 2723–2727 (2021).
- <sup>41</sup>P. Fremdling, *Preparative Mass Spectrometry Instrumentation for Large Native Protein Deposition*, Thesis, University of Oxford (2023).
- <sup>42</sup>A. Punjani, J. L. Rubinstein, D. J. Fleet, and M. A. Brubaker, “cryosparc: algorithms for rapid unsupervised cryo-em structure determination,” *Nature Methods* **14**, 290–296 (2017).
- <sup>43</sup>J. Zivanov, T. Nakane, B. O. Forsberg, D. Kimanius, W. J. H. Hagen, E. Lindahl, and S. H. W. Scheres, “New tools for automated high-resolution cryo-em structure determination in relion-3,” *eLife* **7**, e42166 (2018).
- <sup>44</sup>P. G. Wolynes, “Biomolecular folding in vacuo!!!(?)” *Proceedings of the National Academy of Sciences* **92**, 2426–2427 (1995).
- <sup>45</sup>S.-H. Roh, C. F. Hryc, H.-H. Jeong, X. Fei, J. Jakana, G. H. Lorimer, and W. Chiu, “Subunit conformational variation within individual groel oligomers resolved by cryo-em,” *Proceedings of the National Academy of Sciences* **114**, 8259–8264 (2017).
- <sup>46</sup>T. Croll, “Isolde: a physically realistic environment for model building into low-resolution electron-density maps,” *Acta Crystallographica Section D* **74**, 519–530 (2018).
- <sup>47</sup>P. Emsley, B. Lohkamp, W. G. Scott, and K. Cowtan, “Features and development of coot,” *Acta Crystallographica Section D - Biological Crystallography* **66**, 486–501 (2010).
- <sup>48</sup>D. Liebschner, P. V. Afonine, M. L. Baker, G. Bunkóczi, V. B. Chen, T. I. Croll, B. Hintze, L.-W. Hung, S. Jain, A. J. McCoy, N. W. Moriarty, R. D. Oeffner, B. K. Poon, M. G. Prisant, R. J. Read, J. S. Richardson, D. C. Richardson, M. D. Sammito, O. V. Sobolev, D. H. Stockwell, T. C.

- Terwilliger, A. G. Urzhumtsev, L. L. Videau, C. J. Williams, and P. D. Adams, “Macromolecular structure determination using X-rays, neutrons and electrons: recent developments in *Phenix*,” *Acta Crystallographica Section D* **75**, 861–877 (2019).
- <sup>49</sup>M. F. Bush, Z. Hall, K. Giles, J. Hoyes, C. V. Robinson, and B. T. Ruotolo, “Collision cross sections of proteins and their complexes: A calibration framework and database for gas-phase structural biology,” *Anal. Chem.* **82**, 9557–9565 (2010).
- <sup>50</sup>K. Jeanne Dit Fouque, A. Garabedian, F. Leng, Y.-C. Tse-Dinh, M. E. Ridgeway, M. A. Park, and F. Fernandez-Lima, “Trapped ion mobility spectrometry of native macromolecular assemblies,” *Anal. Chem.* **93**, 2933–2941 (2021).
- <sup>51</sup>C. J. J. Hogan, B. T. Ruotolo, C. V. Robinson, and J. Fernandez de la Mora, “Tandem differential mobility analysis-mass spectrometry reveals partial gas-phase collapse of the groel complex,” *J. Phys. Chem. B* **115**, 3614–3621 (2011).
- <sup>52</sup>E. v. Duijn, A. Barendregt, S. Synowsky, C. Versluis, and A. J. R. Heck, “Chaperonin complexes monitored by ion mobility mass spectrometry,” *J. Am. Chem. Soc.* **131**, 1452–1459 (2009).
- <sup>53</sup>A. Merk, A. Bartesaghi, S. Banerjee, V. Falconieri, P. Rao, M. I. Davis, R. Pragani, M. B. Boxer, L. A. Earl, J. L. S. Milne, and S. Subramaniam, “Breaking cryo-em resolution barriers to facilitate drug discovery,” *Cell* **165**, 1698–1707 (2016).
- <sup>54</sup>M. J. Borgnia, S. Banerjee, A. Merk, D. Matthies, A. Bartesaghi, P. Rao, J. Pierson, L. A. Earl, V. Falconieri, S. Subramaniam, and J. L. S. Milne, “Using cryo-em to map small ligands on dynamic metabolic enzymes: Studies with glutamate dehydrogenase,” *Molecular Pharmacology* **89**, 645–651 (2016).
- <sup>55</sup>J. B. Fenn, “Electrospray wings for molecular elephants (nobel lecture),” *Angewandte Chemie International Edition* **42**, 3871–3894 (2003).
- <sup>56</sup>L. Konermann, E. Ahadi, A. D. Rodriguez, and S. Vahidi, “Unraveling the mechanism of electrospray ionization,” *Analytical Chemistry* **85**, 2–9 (2013).
- <sup>57</sup>K. Anggara, H. Ochner, S. Szilagyi, L. Malavolti, S. Rauschenbach, and K. Kern, “Landing proteins on graphene trampoline preserves their gas-phase folding on the surface,” *ACS Cent. Sci.* **9**, 151–158 (2023).
- <sup>58</sup>J. V. Barth, G. Costantini, and K. Kern, “Engineering atomic and molecular nanostructures at surfaces.” *Nature* **437**, 671–9 (2005).
- <sup>59</sup>S. Carra, S. Alberti, P. A. Arrigo, J. L. Benesch, I. J. Benjamin, W. Boelens, B. Bartelt-Kirbach, B. J. J. M. Brundel, J. Buchner, B. Bukau, J. A. Carver, H. Ecroyd, C. Emanuelsson, S. Finet,

- N. Golenhofen, P. Goloubinoff, N. Gusev, M. Haslbeck, L. E. Hightower, H. H. Kampinga, R. E. Klevit, K. Liberek, H. S. Mchaourab, K. A. McMenimen, A. Poletti, R. Quinlan, S. V. Strelkov, M. E. Toth, E. Vierling, and R. M. Tanguay, “The growing world of small heat shock proteins: from structure to functions,” *Cell Stress and Chaperones* **22**, 601–611 (2017).
- <sup>60</sup>F. Stengel, A. J. Baldwin, A. J. Painter, N. Jaya, E. Basha, L. E. Kay, E. Vierling, C. V. Robinson, and J. L. P. Benesch, “Quaternary dynamics and plasticity underlie small heat shock protein chaperone function,” *Proceedings of the National Academy of Sciences* **107**, 2007–2012 (2010), <https://www.pnas.org/doi/pdf/10.1073/pnas.0910126107>.
- <sup>61</sup>H. Ochner, S. Szilagy, M. Edte, T. K. Esser, S. Rauschenbach, L. Malavolti, and K. Kern, “Imaging conformations of holo- and apo-transferrin on the single-molecule level by low-energy electron holography,” *Scientific Reports* **13**, 10241 (2023).
- <sup>62</sup>L. H. Urner, “Advances in membrane mimetics and mass spectrometry for understanding membrane structure and function,” *Current Opinion in Chemical Biology* **69**, 102157 (2022).
- <sup>63</sup>A. Oluwole, D. Shutin, and J. Bolla, “Mass spectrometry of intact membrane proteins: shifting towards a more native-like context,” *Essays Biochem* **67**, 201–213 (2023).
- <sup>64</sup>J. Fan, C. DeAth, L. Eriksson, C. von Hallerstein, L. J. Persson, A. O. Oluwole, N. Naseeb, A. Qureshi, S. Mesoy, L. T. Seeley, S. B. Knoblauch, N. Kalmankar, E. G. Marklund, T. Esser, C. V. Robinson, L. Baker, and S. Rauschenbach, “Membrane proteins retain native architecture through native esi and soft-landing,” *bioRxiv*, 2026.01.13.699114 (2026).
- <sup>65</sup>W. A. Curtis, J. Hraby, C. R. Krüger, S. V. Barrass, M. Drabbels, and U. J. Lorenz, “Ultrathin liquid cells for microsecond time-resolved cryo-em,” *bioRxiv*, 2025.05.05.652279 (2025).
- <sup>66</sup>U. Flores-Perez and P. Jarvis, “Isolation and suborganellar fractionation of arabidopsis chloroplasts.” *Methods in molecular biology (Clifton, N.J.)* **1511**, 45–60 (2017).
- <sup>67</sup>E. F. Pettersen, T. D. Goddard, C. C. Huang, E. C. Meng, G. S. Couch, T. I. Croll, J. H. Morris, and T. E. Ferrin, “Ucsf chimeraX: Structure visualization for researchers, educators, and developers,” *Protein Science* **30**, 70–82 (2021).
- <sup>68</sup>D. N. Mastrorade, “Automated electron microscope tomography using robust prediction of specimen movements.” *Journal of structural biology* **152**, 36–51 (2005).
- <sup>69</sup>J. R. Kremer, D. N. Mastrorade, and J. R. McIntosh, “Computer visualization of three-dimensional image data using imod.” *Journal of structural biology* **116**, 71–6 (1996).
- <sup>70</sup>S. Kahle, Z. Deng, N. Malinowski, C. Tonnoir, A. Forment-Aliaga, N. Thontasen, G. Rinke, D. Le, V. Turkowski, T. S. Rahman, S. Rauschenbach, M. Ternes, and K. Kern, “The quantum

magnetism of individual manganese-12-acetate molecular magnets anchored at surfaces.” *Nano letters* **12**, 518–21 (2012).

<sup>71</sup>D. Necas and P. Klapetek, “Gwyddion: an open-source software for SPM data analysis,” *Central European Journal of Physics* **10**, 181–188 (2012).